Multiscale dynamics of the Tonga–Kermadec subduction zone

Magali I. Billen,* Michael Gurnis and Mark Simons

Seismological Laboratory, California Institute of Technology, Pasadena, CA 91125, USA

SUMMARY

Our understanding of mantle convection and the motion of plates depends intimately on our understanding of the viscosity structure of the mantle. While geoid and gravity observations have provided fundamental constraints on the radial viscosity structure of the mantle, the influence of short-wavelength variations in viscosity is still poorly understood. We present 2-D and 3-D finite-element models of mantle flow, including strong lateral viscosity variations and local sources of buoyancy, owing to both thermal and compositional effects. We first use generic 2-D models of a subduction zone to investigate how different observations depend on various aspects of the viscosity structure, in particular, the slab and lower-mantle viscosity and the presence of a low-viscosity region in the mantle wedge above the slab. We find that: (1) the strain rate provides a strong constraint on the absolute viscosity of the slab (10^{23} Pa s); (2) stress orientation within the slab is sensitive to the relative viscosity of the slab, lower mantle and the wedge; and (3) the stress state and topography of the overriding plate depend on the wedge viscosity and local sources of buoyancy. In particular, the state of stress in the overriding plate changes from compression to extension with the addition of a low-viscosity wedge. We then use observations of strain rate, stress orientation, dynamic topography and the geoid for the Tonga–Kermadec subduction zone as simultaneous constraints on the viscosity and buoyancy in a 3-D regional dynamic model. Together these observations are used to develop a self-consistent model of the viscosity and buoyancy by taking advantage of the sensitivity of each observation to different aspects of the dynamics, over a broad range of length-scales. The presence of a low-viscosity wedge makes it possible to match observations of shallow dynamic topography and horizontal extension within the backarc, and down-dip compression in the shallow portion of the slab. These results suggest that a low-viscosity wedge plays an important role in controlling the presence of backarc spreading. However, for a model with a low-viscosity and low-density region that provides a good fit to the observed topography, we find that a reduction of the slab density by a factor of 1.3 relative to the reference density model, is required to match the observed geoid. These results suggest that compensation of the slab by dynamic topography may be a much smaller effect at short to intermediate wavelengths than predicted by long-wavelength modelling of the geoid.

Key words: dynamics, lateral heterogeneity, mantle viscosity, subduction.

1 INTRODUCTION

The multiscale nature of dynamics within the Earth is easily seen in the observed geoid (Fig. 1) and bathymetry (Fig. 2) in the region surrounding the Tonga–Kermadec subduction zone. The observed geoid is dominated by a very long-wavelength (>5000 km) increase in geoid height, from east to west and south to north (40–100 m). Superimposed on this long-wavelength signal the Tonga–Kermadec and New Hebrides Trenches are marked by small (10 m),

short-wavelength (~100 km) geoid lows. The observed bathymetry is dominated by short- to intermediate-wavelength (500–1000 km) signals caused by crustal thickness variations, including the continental fragments making up New Zealand (Chatham Rise, Campbell Plateau and Lord Howe Rise), and owing to variation in lithospheric age, including the very young backarc spreading centres above the Tonga–Kermadec and New Hebrides subduction zones (Lau Basin, Havre Trough and Fiji Basins). At shorter wavelengths, the location of remnant and active island arcs (Coleville and Tonga–Tofua Ridges) are apparent, as are the trenches marking the subduction zones. Trenches are the largest signals observed in the bathymetry with depths exceeding 4–5 km relative to abyssal depths. Over the last 5 Myr the Tonga–Kermadec subduction zone has been

*Now at: Woods Hole Oceanographic Institution, Geology and Geophysics, Mailstop no 8, Woods Hole, MA 02543, USA. E-mail: mbillen@whoi.edu
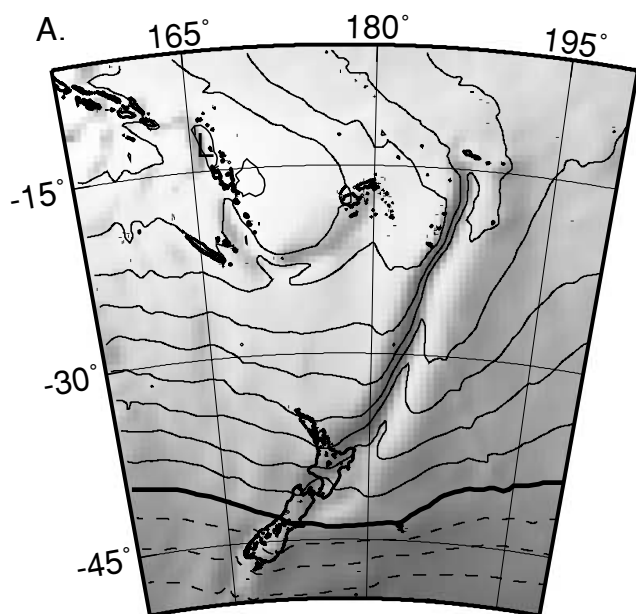
Figure 1. Observed geoid for harmonic degrees $L = 2$–360 for the region of the Tonga–Kermadec subduction zone (Lemoine *et al.* 1998). The contour interval is 10 m (dashed, negative; solid, positive; thick-solid, zero). The grey image highlights smaller-scale relief on the longer-wavelength geoid.
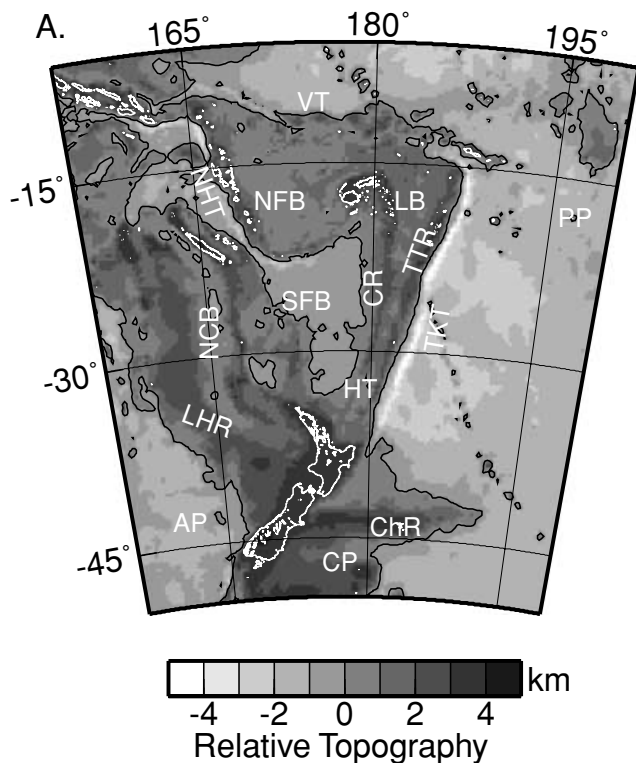
Figure 2. Observed bathymetry for the region of the Tonga–Kermadec subduction zone (GEBCO 1997). Depths are shifted up by 3.5 km, for comparison with model results, placing the abyssal depths of the Pacific Plate at ∼0 km depth (marked by the black contour). TKT, Tonga–Kermadec Trench; NHT, New Hebrides Trench; VT, Vitiaz Trench; CR, Coleville Ridge; TTR, Tonga–Tofua Ridge; LB, Lau Basin; HT, Havre Trough; NFB, North Fiji Basin; SFB, South Fiji Basin; ChR, Chatham Rise; CP, Campbell Plateau; LHR, Lord Howe Rise; NCB, New Caledonia Basin; PP, Pacific Plate; AP, Australian Plate.

characterized by very fast subduction (∼20 cm yr^{-1} total convergence), active backarc spreading and slab rollback. This style of subduction, with several episodes of backarc extension, has been present in the region for at least 45 Ma, creating a series of remnant arcs and extensional basins from the eastern edge of the Lord Howe Rise to the present-day active margin (Kroenke 1984).

While the full spectrum of the dynamic response displayed by these observations reflects the scale of variation in the mantle, in terms of both driving forces and viscosity structure, previous studies of the dynamics have independently focused on the behaviour at either the very longest wavelengths (>5000 km) or the very shortest (100–500 km) wavelengths. Here, we begin to merge the understanding we have gained from these previous studies using finite-element models of mantle flow, including strong variations in viscosity, local sources of buoyancy and a fault interface along plate boundaries, to study the multiscale dynamics in a subduction zone. Our study is motivated by the increasing number of indirect observations (seismic, geochemical, rock mechanics) that indicate local, lateral variations in viscosity may play an important role in the dynamics of subduction zones and mantle convection.

2 DYNAMIC MODELLING CONSTRAINTS ON VISCOSITY

2.1 Long-wavelength geoid and topography

Global modelling of the long-wavelength geoid illustrates the importance of the dynamic response of the mantle, demonstrating the compensation of density anomalies within the mantle by flow-induced deformation of the surface and core–mantle boundaries, and placing strong constraints on the radial structure of viscosity in the mantle. Several studies have shown that the very long-wavelength geoid (harmonic degrees $L = 2$–9) can be explained by a radially stratified viscosity structure (Hager 1984; Richards & Hager 1984; Ricard *et al.* 1988; Vigny *et al.* 1991; Thoraval & Richards 1997; Wen & Anderson 1997). While the details of these studies vary, the main conclusions are: (1) there is an increase in viscosity by a factor of 30–100 from the upper to the lower mantle (Hager 1984; Hager *et al.* 1985; Hager & Clayton 1989; Hager & Richards 1989; Richards & Hager 1984); (2) the $L = 2$–3 variation of the geoid is primarily caused by lower-mantle density anomalies (Hager *et al.* 1985; Hager & Clayton 1989; Hager & Richards 1989); and (3) the $L = 4$–9 variation of the geoid, correlated with the locations of slabs in the upper-mantle, is best fitted by a viscosity structure with a weak lithosphere (Hager 1984; Hager & Clayton 1989).

As discussed by Richards & Hager (1984) and Hager (1984), the total geoid is a sum of the contribution from internal density anomalies, owing to thermal or mineralogical variations, and the contribution from the flow-induced deformation of the boundaries (dynamic topography). While these studies predict up to several kilometres of long-wavelength dynamic topography at the surface, it is difficult to assess whether these predictions match observations, because near-surface density variations at shorter wavelengths, including subduction zones, mask this signal. This creates a fundamental ambiguity in constraining viscosity with only observations of the geoid, as a result of dynamic topography on the boundaries: while the wavelength dependence of the geoid gives some sensitivity to the depth and amplitude of density anomalies, a trade-off remains between the size and location of density anomalies, and the viscosity structure. Seismic tomography can be used to constrain the location of density anomalies (Hager & Clayton 1989). However, the

relationship between seismic velocity anomalies and density depends on temperature and chemical variations, and anharmonic effects, and is not yet well constrained (Karato & Karki 2001).

The models discussed above suggest that density anomalies within the mantle are caused by temperature variations, but ignore the strong temperature dependence of viscosity by including only radial variations in viscosity. This assumption facilitates an analytic solution to the flow, and later studies have argued that small variations in viscosity (less than $10\times$) expected in the lower mantle would have little effect on the very long-wavelength geoid predicted by radially stratified models (Richards & Hager 1989). However, larger variations in viscosity, associated with slabs, continents or weak plate boundaries in the upper mantle, may influence the results at shorter wavelengths ($L > 4$) (Ravine & Morgan 1993; Zhang & Christensen 1993). An example of the possible influence of lateral variations on the inferred radial structure is the result that the correlation of the geoid with slabs is improved by a radial viscosity structure with a weak lithosphere and that this difference in the inferred viscosity structure may be caused by locally weak plate boundaries above slabs (Hager 1984). In addition, Koch & Ribe (1989) found that ignoring the strength of the slabs may underestimate surface deformation and therefore lead to an underestimate of the jump in the viscosity from the upper to the lower mantle.

Numerical models of viscous flow have been used to investigate the influence of large ($10-10^4$) lateral variations in viscosity (Sabadini *et al.* 1992; Moresi & Gurnis 1996; Zhong & Davies 1999). In a 3-D model of the Mariana subduction zone, Moresi & Gurnis (1996) found that a jump in viscosity, from the upper to the lower mantle, larger than predicted by radial models, was needed if a slab in contact with the lower mantle was stronger than the surrounding asthenosphere. However, they were not able to match the observed short-wavelength geoid or the long- or short-wavelength dynamic topography. This result demonstrates a disturbing reality of inferring a multiscale viscosity structure from the geoid: the response of the long-wavelength geoid to lateral variations in viscosity is not unique and a reasonable fit to the geoid is possible even when the dynamic topography does not agree with observations. This suggests that it is necessary to use multiple observations as simultaneous constraints on the 3-D viscosity structure.

2.2 Short-wavelength topography and gravity

Modelling of topography in subduction zones has traditionally focused on the flexural response of the lithosphere as either an elastic, viscous or elasto-plastic plate subject to a force or displacement near the trench (DeBremaecker 1977; Melosh 1978; Turcotte *et al.* 1978; Bodine & Watts 1979). These models successfully recreate the morphology of the trench, including the forebulge. However, since the influence of slab buoyancy and flow in the mantle are not included, this approach cannot be used to infer the viscosity structure or driving forces responsible for forming the trench. Kinematic and dynamic numerical models of viscous flow have been used to investigate the causes of short-wavelength topography and gravity in subduction zones (Sleep 1975; McAdoo 1982). Sleep (1975) attempts to model the topography and gravity for the Aleutian subduction zone using numerical models of 2-D Newtonian viscous flow. These models include crustal thickness variations based on seismic observations, the slab buoyancy based on the location of seismicity, temperature-dependent viscosity and weak zones along the plate boundary and beneath the island arc. A match to both the gravity and topography was not found in part because the plate boundary

was modelled as a weak zone without a fault and required a very dense slab to match the trench depth.

Dynamic models of viscous flow in subduction zones that include a fault along the plate boundary have successfully reproduced trench morphology (Zhong & Gurnis 1992; Zhong & Gurnis 1994; Zhong *et al.* 1998; Buiter *et al.* 2001) and the long-wavelength geoid (Zhong & Gurnis 1992). These models include radial and temperature-dependent Newtonian or non-Newtonian viscosity, density anomalies arising from the thermal anomaly of the slab and, in some cases, crustal thickness variations on the overriding plate (Zhong & Gurnis 1994). However, contrary to observations, these models predict a large depression (3–4 km) in dynamic topography on the overriding plate (in the arc/backarc region) and a short-wavelength depression in the geoid or gravity over the backarc region. Similar results for topography are found in models including visco-elastic rheology, with only a slightly longer-wavelength depression in the backarc region (Gurnis *et al.* 1996). Billen & Gurnis (2001) demonstrate that this deep basin can be eliminated by including a low-viscosity region in the wedge, thereby decoupling the flow of the slab from the overriding plate.

2.3 Seismological constraints on viscosity

The viscous strength of the slab is an important parameter coupling flow in the mantle to the observed deformation on the surface. However, it is not only difficult to isolate the viscosity of the slab from other viscosity variations using only topography and geoid, it is not possible to infer the absolute viscosity of the slab. Several dynamic studies conclude that the lithosphere weakens as it bends at the trench and subducts into the mantle (Zhong *et al.* 1996; Conrad & Hager 1999). However, the occurrence of seismicity within slabs to depths of 670 km implies that the slab retains some strength throughout the upper mantle. Observations of strain rate and stress orientation inferred from seismicity and moment tensor solutions provide additional constraints on the strength of slabs, and coupling of slabs to the higher-viscosity lower mantle.

Earthquakes provide an indirect measure of the strain release within areas of distributed deformation and a lower bound on the strain rate within the mantle. The strain rate, $\dot{\epsilon}$, as a result of earthquakes, can be estimated as $\dot{\epsilon} = \sum M_o / 2\mu V t$, where $M_o = \mu A D$ is the moment for a single earthquake (μ is the elastic shear modulus, A is the area of the fault, D is the average slip over A) and $\sum M_o$ is the cumulative seismic moment release within a volume V, occurring over a timespan t (Kostrov 1974). Bevis (1988) uses this model of strain-rate release from earthquakes to estimate the strain rate in slabs to be of the order of 1×10^{-15} s^{-1} at between 75 and 175 km depth. Holt (1995) and Nothard *et al.* (1996) find similar strain rates for a portion of the Tonga slab down to 200 km depth, with slightly smaller strain rates (5×10^{-16} s^{-1}) between 200 and 650 km. These estimates of the minimum strain rate in the slab provide an important constraint on the viscosity of the slab in dynamic models.

The orientation of stress within slabs, based on compressional and tensional axes of earthquake focal mechanisms, provides another constraint on the strength of slabs and the lower mantle. Most slabs with seismicity extending to 670 km depth are in down-dip or vertical tension in the upper 300 km and compression below 300 km (Isacks & Molnar 1971). The Tonga–Kermadec and Izu–Bonin slabs are important exceptions, appearing to be in down-dip compression throughout (Isacks & Molnar 1971; Apperson & Frohlich 1987; Seno & Yamanaka 1998). Vassiliou *et al.* (1984) show that stress

orientations and distribution of the number of earthquakes with depth (a gradual decrease from the surface to 300 km, a minimum between 300 and 400 km and an increase from 400 to 670 km), at most subduction zones, are consistent with a slab sinking under its own weight and meeting a substantial resistance to flow at a depth of 670 km. Regional studies also show that seismic strain rate has the same depth distribution as the number of earthquakes within the slab (Holt 1995; Nothard *et al.* 1996).

3 THE SUBDUCTION ZONE WEDGE

The wedge in a subduction zone, the region above a subducting plate and beneath the overriding plate, is probably the location of strong lateral variations in viscosity and buoyancy owing to processes involving fluids released by the subducting slab and subsequent metasomatism and melting. Previous models have incorporated the exponential dependence of viscosity on temperature, pressure and mineralogical variations in viscosity, in terms of radially stratified viscosity structure, and stress-dependent viscosity in terms of non-Newtonian flow laws. However, the influence of melt and water on viscosity has largely been ignored owing to the challenges in explicitly including such variations and the lack of experimental and theoretical constraints on its influence. However, Davies & Stevenson (1992) demonstrated that local variations in viscosity or buoyancy may strongly affect flow in the wedge.

3.1 Evidence of a low-viscosity wedge

Recently, experimental and theoretical research on the rheological behaviour of olivine at conditions applicable to the upper mantle has made it possible to use seismic observations to constrain the location of fluids in the upper mantle and to begin quantifying the effects of these fluids on viscosity. Geochemical and petrologic data indicate that fluids are incorporated into the wedge owing to dehydration of the subducting slab (Tatsumi *et al.* 1983; Morris *et al.* 1990; Stolper & Newman 1994). Tatsumi *et al.* (1983) find that the chemical composition of primary magmas for the Northeast Japan Arc formed in the presence of 3 wt per cent water. Stolper & Newman (1994) explain the composition of Mariana Trough and Island Arc magmas in terms of mixing of a normal mid-ocean ridge basalt (NMORB) source (infertile peridotite) with an H_2O-rich component, and attribute the increase in degree of melting, from the backarc to the island arc, to the result of an increase in the amount of water in the wedge towards the island arc. Morris *et al.* (1990) show that the source for water in island-arc magmas is water carried down by the slab, by tracing the elements B and Be in the magmas to sediments on the down-going plate.

Experimental studies of rheology at low pressures (<300 MPa) show that the viscosity of olivine aggregates decreases approximately linearly with increasing water content (Mei 1999; Karato 2003). While the rheology of minerals at higher pressures has been poorly constrained, a recent study at 2 GPa has established a quantitative flow law for olivine that can be extrapolated to higher pressure (Karato & Jung 2003). This work, combined with the results on pressure dependence of hydroxyl solubility in olivine (Kohlstedt *et al.* 1996), suggests that the weakening effects of water will be even greater at the higher water fugacity conditions probable in the deep upper mantle of a subduction zone.

Seismic studies in subduction zones reveal anomalies of low velocity (Hasegawa *et al.* 1991; Roth *et al.* 2000) and high attenuation (Barazangi & Isacks 1971; Roth *et al.* 2000) in the wedge, consistent with the presence of volatiles, particularly water (Karato & Jung 1998) and possibly melt. Tomography studies for the Northeast Japan subduction zone reveal a −4 to −6 per cent *P*-wave velocity anomaly in the uppermost mantle, immediately beneath the arc crust, and continuous along the strike of the arc (Zhao *et al.* 1992). Similar anomalies of −2 to −6 per cent are found in regional tomography models of the Tonga–Kermadec subduction zone (Zhao *et al.* 1997). Observations of high attenuation (low *Q*) accompany observations of low seismic velocity in Northeast Japan and Tonga–Kermadec (Barazangi & Isacks 1971; Roth *et al.* 1999). Further evidence for volatiles in the wedge is found in the Cascadia subduction zone, where very low shear wave velocities are found along planar structures above the slab in the forearc region, consistent with hydrated and serpentinized mantle (Bostock *et al.* 2002).

While spatial resolution in seismic attenuation models is much less than in seismic velocity models, regions of high attenuation (low *Q*) and low seismic velocity appear to be correlated in these subduction zones. Using the results of Karato (2003) the low seismic velocity (−4 to −6 per cent) and high attenuation regions found above the Northeast Japan and Tonga–Kermadec slabs indicate water concentrations of at least 3000 $H/10^6$ Si, if the associated temperature anomalies are ∼200 K. These water concentrations are three times those inferred for the oceanic asthenosphere under mid-ocean ridges.

In addition to experimental evidence for the weakening effects of water at relatively low pressures, Karato (2003) presents a relationship between viscosity and seismic attenuation and velocity. This relationship, which assumes that the kinetics of both attenuation and steady-state creep are affected by water through the same mechanism (i.e. weakening arising from hydrogen-related defects), provides a quantitative method by which seismic observations can be used to map the viscosity structure of the mantle. For the low seismic velocity (−2 to −5 per cent for *P* waves) and high attenuation regions of the wedge, this relationship predicts a decrease in viscosity of two to four orders of magnitude.

At shallow depths in the wedge (<100 km), observations of low seismic velocity are more probably caused by a relatively high melt fraction beneath the active island arc. In mid-ocean ridge environments, the low water content and low pressures of melting lead to an increase in viscosity in the residue of melting, as water is fully partitioned into the melt and the melt fraction is not high enough to decrease the viscosity (Hirth & Kohlstedt 1996). Depending on the degree of melting and flux of volatiles from the subducting slab, experimental evidence on the influence of melt on the rheology of olivine aggregates, indicates that where there is a high melt fraction, the viscosity of the mantle decreases exponentially with increasing melt content (Kelemen *et al.* 1997). Therefore, these shallow low seismic velocity regions in the wedge may also be low-viscosity regions.

These observations and experiments suggest that the viscosity in the wedge, extending from the top of the subducted slab at depths of 100–200 km to the base of the overriding crust, may be substantially less than the background asthenosphere and mantle lithosphere. Such a low-viscosity wedge (LVW) will affect the flow in the wedge and deformation of the overriding plate.

3.2 Sources of buoyancy in the wedge

Density variations within the wedge may result from processes associated with the extensive flux of volatiles from the slab, induced melting beneath the backarc and island arc, and subsequent depletion of the source region for magmas. The main effect of water

fluxing into the wedge is to increase the degree of melting by decreasing the solidus temperature. Above the wet solidus, in regions of high melt fraction, the density in the wedge may decrease by 5–20 kg m^{-3} for an *in situ* melt fraction of 1–4 per cent (the density of the melt, ignoring variations with depth, will be approximately 500 kg m^{-3} less than the surrounding rock). Continual fluxing of water into the wedge also leads to larger degrees of melting and can lead to a decrease in density of the residue remaining in the wedge. Stolper & Newman (1994) found that the degree of melting increased from 5 to 17 wt per cent for the Mariana backarc to greater than 30 wt per cent for Mariana island-arc magmas. Such high degrees of melting lead to lower Al$_2$O$_3$ contents in the residue. At low pressures ($P < 10$ kbar), in the spinel stability field, this leads to little change in density. However, if this residue is transported into the garnet stability field ($P > 30$ kbar) by flow in the wedge, the low Al$_2$O$_3$ content limits the amount of garnet that forms. This results in a 10–20 kg m^{-3} decrease in the density, relative to peridotite that has undergone only 10 wt per cent melting, and a density decrease of up to 50 kg m^{-3} compared with fertile peridotite (P. Asimow, private communication, 2001).

While density variations in the crust or at the base of the crust as a result of melt will contribute to dynamic topography, these variations are isostatically compensated, and therefore do not contribute significantly to the geoid or gravity. However, density anomalies in the deeper (100–200 km) regions of the wedge, caused by extensive depletion of peridotite, could contribute significantly to both dynamic topography and the geoid.

4 NUMERICAL METHOD

We develop a model of instantaneous dynamic flow, which allows us to focus on the effects of lateral variations in viscosity on deformation in a subduction zone. From the velocity and pressure we calculate topography, geoid, stress orientations and strain rate, to characterize those viscosity structures that are consistent with the general form of deformation observed at the world's subduction zones, and the particular case of the Tonga–Kermadec subduction zone.

Flow in the mantle is governed by the equations for conservation of mass and momentum. For the mantle, with a very high Prandtl number, inertial forces are negligible. We use the Boussinesq approximation, which ignores all variations in density except in the body force term in the momentum equation. With these assumptions the equations for conservation of mass and momentum reduce to the continuity equation,

$$\nabla \cdot \mathbf{u} = 0, \tag{1}$$

and the Stokes equation,

$$\nabla \cdot \sigma + \mathbf{f} = 0, \tag{2}$$

where $\mathbf{u}$, $\mathbf{f}$ and σ are the flow velocity, the body force and stress tensor, respectively. The body force includes density anomalies as a result of temperature T (inferred density variations owing to the composition of the crust are included in terms of equivalent temperature),

$$f_i = \rho_o \alpha (T - T_o) g \delta_{ir}, \tag{3}$$

where ρ_o is the reference density, T_o is the reference temperature, g is the gravitational acceleration, α is the coefficient of thermal expansion and δ_{ij} is the Kronecker delta.

The stress tensor defines the constitutive relation,

$$\sigma_{ij} = -P\delta_{ij} + \eta\dot{\epsilon}_{ij}, \tag{4}$$

where P is the pressure, η is the dynamic viscosity and $\dot{\epsilon}_{ij}$ is the strain-rate tensor in spherical coordinates given by

$$\dot{\epsilon}_{ij} = (u_{i,j} + u_{j,i}), \tag{5}$$

where $u_i \equiv (u_\phi, u_r, u_\theta)$, $X_{,y}$ denotes the derivative of X with respect to y, i and j are spatial indices and the spatial coordinates (x_i) are longitude, ϕ, radius, r, and latitude, θ. Making the following change of variables:

$$x_i = R x_i' \quad u_i = \frac{\kappa}{R} u_i'$$
$$P = \frac{\eta_o \kappa}{R^2} P' \quad \eta = \eta_o \eta',$$
$$T = T_o + \Delta T \, T' \tag{6}$$

where R is the radius of the Earth, κ is the thermal diffusivity, η_o is the reference viscosity and ΔT is the temperature difference between the top surface and the interior of the mantle, and substituting eqs (3) and (4) into eq. (2), the equations of motion become

$$u_{i,i}' = 0, \tag{7}$$

and

$$-P_{,j}' \delta_{ij} + (\eta' u_{i,j}' + \eta' u_{j,i}')_{,j} + Ra\, T' \delta_{ir} = 0, \tag{8}$$

where

$$Ra = \frac{\rho_o g \alpha \Delta T R^3}{\eta_o \kappa} \tag{9}$$

is the Rayleigh number, which depends on the choice of physical parameters for the Earth's mantle. Note, that in solving for the instantaneous flow, we do not solve the energy equation, and therefore this is a quasi-dynamic (rather than a fully dynamic) solution.

The values for the physical parameters used in most of the models are summarized in Table 1. For models in which other parameters are used, the differing parameters will be indicated.

The viscosity is radially, laterally and temperature dependent. Radially, the mantle is divided into four layers: lithosphere (0–100 km), asthenosphere (100–410 km), transition zone (410–670 km) and lower mantle (670–2890 km). The temperature dependence of the non-dimensional viscosity in each layer is given by

$$\eta'(r', T') = \eta^*(r, \phi, \theta) \exp\left(\frac{c_1}{T' + c_2} - \frac{c_1}{1 + c_2}\right), \tag{10}$$

where the constants c_1, c_2 and $\eta^*(r, \theta, \phi)$ can differ in each layer. The parameter c_1 accounts for the activation energy in the non-dimensional viscosity law, while the parameter c_2 accounts for the non-dimensional temperature and temperature offset at the surface. Lateral variations in viscosity not caused by temperature variations are included by setting c_1 and c_2 to zero and η^* to the desired viscosity.

Table 1. Model parameters.

Variable name		Value
Reference density	ρ_o	3300 kg m^{-3}
Temperature difference between the top and bottom surface	ΔT	1500 K
Thermal diffusivity	κ	1×10^{-6} m^2 s^{-1}
Coefficient of thermal expansion	α	2×10^{-5} K^{-1}
Earth radius	R	6371.137 km
Gravitational acceleration	g	10 m s^{-2}
Reference viscosity	η_o	3×10^{20} Pa s
Rayleigh number	Ra	8.53×10^8

The choice of η_o is not immediately obvious for a fully 3-D viscosity structure. The Stokes equation expresses a balance of buoyancy and viscous forces that depends on the velocity. In this balance the magnitude of the velocity scales inversely with η_o, while the distribution of flow and pressure will depend only on the relative viscosity within the model. Since our aim is to study variations in the viscosity structure, it is important to choose η_o to coincide with a region for which the viscosity is the same for all the models, so that comparisons of stress and topography are straightforward. We choose to have η_o coincide with the asthenosphere viscosity η_{asth}. Implicit in this choice is the assumption that the viscosity of the asthenosphere is important in determining the magnitude of flow in the upper mantle and, in particular, in the slab. We will return to this assumption later, as we will find that η_{asth} is not controlling the vigour of convection in the upper mantle in models driven by the buoyancy of the slab.

In the model formulation described above, we choose to use a purely viscous rheology and do not include the elastic behaviour of the shallow lithosphere. Elasticity is an important property of the lithosphere at short timescales (e.g. earthquakes) and short wavelengths (e.g. redistributing dynamic support of short-wavelength loads over longer wavelengths). However, the instantaneous models we use are analogous to long-timescale, steady-state solutions. Therefore, the main effect of elasticity in the lithosphere would be to dampen the very short-wavelength topographic features caused by regional compensation. In addition, DeBremaecker (1977) and Melosh (1978) showed that the load of the slab on the lithosphere could be supported by purely viscous stresses and Gurnis *et al.* (1996) showed that there is little difference in the topography for models including visco-elasticity compared with models with purely viscous rheology.

4.1 Model domain and boundary conditions

The equations of motion are solved for the velocity and pressure by the finite-element code CitcomT, designed to study 3-D dynamic models in a region of a sphere. CitcomT has been modified from the Cartesian geometry code Citcom (Moresi & Solomatov 1995; Moresi & Gurnis 1996; Zhong *et al.* 1998) using a coordinate transformation to spherical geometry (see Appendix A). The model domain extends from the surface to the core–mantle boundary (Fig. 3). 3-D models of the Tonga–Kermadec region extend 45° in longitude (155°–200°) and latitude (5°–50°S) where the sidewalls of the domain are lines of equal longitude or latitude. The top and bottom surfaces have free-slip ($u_{rr} = 0$, $\sigma_{r\theta} = \sigma_{r\phi} = 0$), isothermal boundary conditions. The sidewalls have reflecting boundary conditions ($u_{\theta\theta} = 0$ or $u_{\phi\phi} = 0$, and $\sigma_{r\theta} = \sigma_{r\phi} = 0$). 2-D models used for investigating the general behaviour of the flow with lateral variations in viscosity are taken from an east–west 2-D cross-section through the 3-D model at a latitude of 28°S.

A fault along the subduction zone boundary within the lithosphere is modelled with boundary conditions requiring continuous normal velocity on the fault interface but allowing discontinuous tangential velocity (Appendix A.3). The fault interface lies along a single plane of element boundaries within the mesh. The varying strike and dip of the fault in 3-D requires that this surface of elements is deformed to match the fault geometry.

In addition, modelling with strong variations in viscosity over short length-scales requires the mesh to have high resolution in these regions. Viscosity variations across a single element are constrained to be less than a factor of 3 for numerical accuracy. Moresi *et al.* (1996) find that accuracy does not depend on the global viscosity
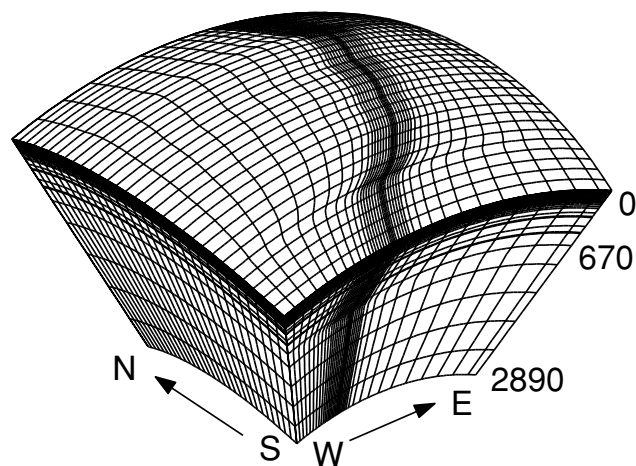
Figure 3. A 3-D View of the Mesh and model Domain. The model domain extends from the surface to the core–mantle boundary, −5° to −50° in latitude and 155° to 200° in longitude. The mesh shown is sampled at every third row of nodes. The mesh has uniform spacing in latitude, every 0.5°. The resolution in depth varies from 2.5 km near the surface to 100 km below 670 km, with increased resolution at depths of 410 and 670 km. The resolution in longitude ranges from 2.5 km near the fault and slab to 100 km at the east and west boundaries of the domain. The high-resolution regions follow the contours of the slab.

variation but rather on gradients within individual elements: the error exceeds 1 per cent if the viscosity varies by more than a factor of 2 or 3 within an element. This means that an order of magnitude variation in viscosity is spread across three elements. To facilitate viscosity variations of several orders of magnitude over a few tens of kilometres, we use a mesh with resolution that varies from 2.5 to 100 km, with the highest resolution in the wedge and along the top surface of the slab.

4.2 Density structure

The main driving force for deformation in the subduction zone is the negative buoyancy of the slab. However, other density anomalies, arising from variations in the age of the lithosphere, crustal thickness, phase change boundaries and compositional differences, may also have an important influence on the flow, topography and geoid. The slab buoyancy in our models is derived from a kinematic model of flow constrained to follow the location of the slab, delineated by seismicity, from the surface to a depth of ~670 km (see Appendix C). The maximum density anomaly within the slab is ~66 kg m^{-3} (using the parameters in Table 1). It is important to include variations in the age of the lithosphere and crustal thickness since the density anomalies associated with both of these variations can contribute to isostatically compensated topography and dynamic topography through induced flow. Age variations within the Tonga–Kermadec model range from 0 Ma along the active backarc spreading system in the Lau and Havre Basins to greater than 100 Ma on the Pacific Plate.

Crustal thickness variations for the continental region (New Zealand, Chatham Rise, Campbell Plateau and Lord Howe Rise), remnant arc (Lau–Coleville Ridge) and active Tonga–Tofua Arc (Raitt *et al.* 1955) are also included in the 3-D models. We do not include density variations arising from the phase changes at 410 and 670 km. Recent studies suggest that the cold temperature within the slab may inhibit the transformation of olivine to spinel at 410 km, leading to little net change in density or a decrease in the density of

the slab relative to the mantle (Stein & Stein 1996). In addition, as we discuss later, we find that the density of the slab caused by temperature may be too high to match observations of the geoid, and the exothermic phase change at 410 km will only further increase the discrepancy we find. The final source of density variations is compositional differences, including the many processes in the mantle wedge that may lead to differences in the density of the wedge: the presence of melt, compositional changes caused by extensive melting and the presence of water (see Section 3.2). We do not attempt to include the processes that lead to the density variations. Instead we focus on how the density variations resulting from these processes might influence the flow, surface deformation and the geoid.

In most of the models presented, we do not include the density anomaly caused by the subducting basaltic crust. Below the basalt-to-eclogite transition, which occurs between 40 and 80 km depth, there is no density difference between the slab and the surrounding mantle caused by the composition. Above this transition, while the density difference between basalt and harzburgite or lherzolite is large (295 and 360 kg m^{-3} Ringwood 1982), the volume of basaltic crust is small. Therefore, the small region of low-density material will contribute to the short-wavelength geoid and topography, directly above the trench, but this effect is expected to contribute less than 2 m to the geoid. We do present one model that includes a delayed basalt–eclogite transition to a depth of 150 km (Section 6), which is possible for a very cold slab (Peacock & Wang 1999).

4.3 Surface observables

The topography and geoid are determined from the non-dimensional velocity and pressure. The non-dimensional dynamic topography, h', on the top or bottom surfaces, balances the normal stress on that surface,

$$h' = \sigma'_{rr}, \tag{11}$$

where $\sigma_{rr} = (\eta_o \kappa / R^2) \sigma'_{rr}$. To dimensionalize the dynamic topography we assume that the surface is everywhere covered by water (this underestimates the topography over the continents that reach above sea level), then

$$h = \frac{\eta_o \kappa}{\Delta \rho g R^2} \sigma'_{rr}, \tag{12}$$

where $\Delta \rho = \rho_o - \rho_w = 2300$ kg m^{-3} is the density contrast between the lithosphere and water.

An accurate determination of dynamic topography is especially important in determining the geoid, which depends on the small difference in the potential owing to density anomalies in the interior and density anomalies owing to surface deformation. We calculate topography using the consistent boundary flux method (Zhong *et al.* 1993). Extensive testing of the topography calculation demonstrates that the topography is accurately determined, in the presence of strong radial or lateral variations in viscosity, with errors of less than 1 per cent (Appendix B).

An important constraint on the validity of our dynamic models is agreement with the observed geoid height, N or gravity anomaly, δg. The observed geoid height and gravity anomaly are commonly expressed in terms of coefficients of a finite sum of surface spherical harmonic functions (e.g. Lambeck 1988). Several techniques for analysis of the geoid take explicit advantage of the spherical harmonic representation of these fields. Therefore, we solve directly for the harmonic coefficients of the geoid height. Density anomalies within the domain are converted to mass sheets at each layer of nodes within the model and integrated to form the potential field

response at the surface. Similarly, topography on the top surface and core–mantle boundary, are converted to equivalent mass sheets.

The spherical harmonic functions used in calculating the geoid are defined for a whole sphere. Therefore, using these functions to calculate the geoid or gravity within our regional domain implicitly assumes that there are no density anomalies outside our domain. This means that if there are density anomalies or non-zero topography along the boundaries of the model, there is, in effect, a step discontinuity along the boundary, which would lead to a large short-wavelength signal in the geoid or gravity. To avoid this contamination of the predicted geoid and gravity, we taper density anomalies to zero at 500 km from the domain boundaries (the age of the lithosphere along the boundary is set to 80 Ma) and the topography is shifted by the mean value along the edge of the domain, to minimize any offset across the model boundaries prior to computing the geoid height or gravity anomaly. An analysis of the geoid is carried out using a wavelength- and position-dependent localization method (Simons 1996, see Section 6.4).

5 2-D MODELS OF SUBDUCTION ZONE DYNAMICS

We begin with 2-D generic models of instantaneous dynamic flow in a subduction zone and explore the influence of both radial and lateral variations in viscosity on topography, velocity, strain rate and stress orientation. The results are first presented in Section 5.1 for models with only radial- and temperature-dependent viscosity (i.e. all lateral variations in viscosity are caused by temperature). These models are listed in Table 2. A subset of these models, including a low-viscosity and a buoyant region in the wedge, is further investigated in Sections 5.2 and 5.3, respectively.

5.1 Radial and temperature-dependent viscosity models

Models with radial and temperature dependence include five independent viscosity parameters: lithosphere, η_{lith}, slab, η_{slab}, asthenosphere, η_{asth}, transition zone, η_{tran}, and lower-mantle, η_{lm}, viscosity. As stated earlier, the asthenosphere viscosity is taken as the reference viscosity (η_o), therefore all viscosity parameters are scaled by this value. This is an important point: velocity (as is strain rate) depends on η_o and is sensitive to both the absolute and relative values of the viscosity in the model. However, the pressure (stress and topography) does not depend directly on η_o and is therefore only dependent on the relative variations of viscosity within the model. The models presented use a reference viscosity of 3×10^{20} Pa s, unless otherwise noted. The lithosphere, slab, transition zone and lower-mantle viscosity vary over several orders of magnitude (Table 2). We limit the number of possible models by requiring that $\eta_{\text{slab}} \geq \eta_{\text{tran}}$, $\eta_{\text{slab}} \leq \eta_{\text{lith}}$ and $\eta_{\text{tran}} \leq \eta_{lm}$, consistent with previous results for the radial viscosity structure of the mantle (King 1995). In addition to the effects of temperature-dependent viscosity associated with the slab, we investigate the influence of the age of the overriding plate, which contributes to lateral variations in viscosity arising from variations in lithosphere thickness.

Basin depth

As found previously (Zhong & Gurnis 1992, 1994; Moresi & Gurnis 1996; Zhong *et al.* 1998), a large basin forms on the overriding plate for all models with only radial- and temperature-dependent viscosity (Table 2), with depths varying from 6 to 26 km.

Table 2. Model viscosity parameters are relative to the reference viscosity (η_o): values listed are log$_{10}$ for each ratio. h_{basin}, depth of the basin on the overriding plate. h_f, forearc height. $\dot{\epsilon}$, volume-averaged second-invariant of the strain-rate tensor within the slab below 100 km. M, plate mobility defined in the text. Models 1a–11c: $\eta_o = 3 \times 10^{20}$ Pa s, Ra=8.58×10^8, lithosphere age is 50 Ma. Models 4ayl–4byl: $\eta_o = 3 \times 10^{20}$ Pa s, Ra = 8.53×10^8, lithosphere age is 0–100 Ma. Model 12: $\eta_o = 3 \times 10^{21}$ Pa s, Ra = 8.53×10^7, lithosphere age is 50 Ma (compare with 5c). Model 13: $\eta_o = 3 \times 10^{19}$ Pa s, Ra = 8.53×10^9, lithosphere age is 50 Ma (compare with 4b).

| Model	η_{slab}/η_o	η_{lith}/η_{slab}	η_{lm}/η_{slab}	η_{tran}/η_{lm}	h_{basin} (km)	h_f (km)	$\dot{\epsilon}$ (s^{-1})	$\bar{\sigma}$ (MPa)	M
				2-D radial and temperature-dependent viscosity models					
1a	0	2	2	−2	−6.5	0.0	2.6×10^{-14}	7.9	8
1b	1	1	1	−2	−6.6	0.0	4.6×10^{-15}	13.8	37
1c	2	0	0	−2	−7.4	0.05	9.6×10^{-16}	28.2	70
2a	0	3	2	−2	−6.7	0.0	2.5×10^{-14}	7.5	1
2b	1	2	1	−2	−7.2	0.0	4.2×10^{-15}	12.6	5
2c	2	1	0	−2	−8.5	0.0	8.1×10^{-16}	24.3	21
2d	3	0	−1	−2	−11.3	0.10	1.9×10^{-16}	59.4	49
3a	0	4	2	−2	−6.9	0.0	2.4×10^{-14}	7.2	0
3b	1	3	1	−2	−7.3	0.0	4.1×10^{-15}	12.2	1
3c	2	2	0	−2	−8.8	0.0	7.8×10^{-16}	23.4	3
3d	3	1	−1	−2	−11.9	0.0	1.9×10^{-16}	57.0	9
3e	4	0	−2	−2	−15.9	0.8	3.7×10^{-17}	113.4	17
4a	1	1	1	−1	−6.3	0.0	3.8×10^{-15}	11.5	41
4b	2	0	0	−1	−6.9	0.0	8.4×10^{-16}	25.1	78
5a	1	2	1	−1	−7.1	0.0	3.6×10^{-15}	10.7	7
5b	2	1	0	−1	−8.3	0.0	7.1×10^{-16}	21.4	25
5c	3	0	−1	−1	−11.0	0.03	1.8×10^{-16}	54.3	54
6a	1	3	1	−1	−7.2	0.0	3.4×10^{-15}	10.3	1
6b	2	2	0	−1	−8.6	0.0	6.9×10^{-16}	20.8	3
6c	3	1	−1	−1	−11.6	0.0	1.7×10^{-16}	51.0	10
6d	4	0	−2	−1	−15.5	0.6	3.5×10^{-17}	104.4	18
7a	2	0	0	0	−6.4	0.1	7.2×10^{-16}	21.6	80
8a	2	1	0	0	−8.0	0.0	6.4×10^{-16}	19.3	28
8b	3	0	−1	0	−10.5	0.0	1.7×10^{-16}	49.5	59
9a	2	2	0	0	−8.5	0.0	6.3×10^{-16}	18.9	4
9b	3	1	−1	0	−11.3	0.0	1.5×10^{-16}	45.6	13
9c	4	0	−2	0	−14.8	0.4	3.1×10^{-17}	93.0	22
10a	2	2	−1	−1	−10.5	0.0	1.4×10^{-15}	40.8	1
10b	3	1	−2	−1	−13.7	0.4	2.8×10^{-16}	84.0	3
10c	4	0	−3	−1	−19.2	2.4	5.3×10^{-17}	158.7	6
11a	2	2	−2	0	−11.1	0.05	1.7×10^{-15}	51.9	1
11b	3	1	−3	0	−15.0	1.3	3.5×10^{-16}	105.0	1
11c	4	0	−4	0	−21.7	4.5	6.7×10^{-17}	200.7	4
4ayl	1	1	1	−1	−7.1	0.1	4.2×10^{-15}	12.6	41
4byl	2	0	0	−1	−8.1	0.4	8.6×10^{-16}	25.7	80
5ayl	1	2	1	−1	−8.6	0.0	3.9×10^{-15}	11.9	7
5byl	2	1	0	−1	−11.5	0.2	7.6×10^{-16}	22.7	26
5cyl	3	0	−1	−1	−16.1	0.7	1.8×10^{-16}	55.2	56
6ayl	1	3	1	−1	−9.6	0.0	3.8×10^{-15}	11.4	1
6byl	2	2	0	−1	−13.4	0.1	7.5×10^{-16}	22.4	4
6cyl	3	1	−1	−1	−20.7	0.7	1.8×10^{-16}	53.7	11
6dyl	4	0	−2	−1	−26.4	2.4	3.9×10^{-17}	115.5	18
12	2	0	0	−1	−7.5	0.03	1.6×10^{-16}	48	54
13	3	0	−1	−1	−6.0	0.0	8.9×10^{-16}	26.7	74

The basin depth increases with increasing strength of the slab, with second-order dependence on the viscosity of the lithosphere, lower mantle or transition zone (Fig. 4). Slab viscosity affects the dynamic topography of the overriding plate by influencing the magnitude of the pressure above the slab. Sinking of the dense slab creates a region of low pressure above the slab and high pressure below the slab. (Note, the pressure is only known to within an arbitrary constant, so we only know the relative magnitude of the pressure.) Low pressure corresponds to suction into the region, which pulls down on the surface to form the basin. The magnitude of the low-pressure region above the slab depends on the relative viscosity of the slab and overlying asthenosphere and the density of the slab. In all of these models the density of the slab is fixed, therefore an increase in slab viscosity, relative to the asthenosphere leads to lower pressure above the slab, which reaches the surface forming a larger basin.

Forebulge

A forebulge on the downgoing plate, ranging in size from ∼100 m to greater than 4 km, forms in two cases. First, for models with a strong lower mantle ($\eta_{lm}/\eta_o = 100$), a forebulge forms when the slab and lithosphere viscosity are equal (Fig. 5). Secondly, a forebulge forms in all models with either a weak (10×) or no jump in viscosity from the transition zone to the lower mantle. As first demonstrated by
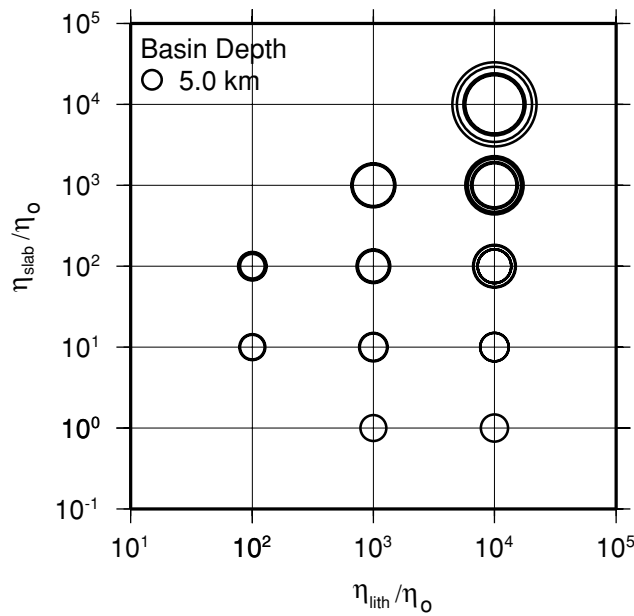
Figure 4. Basin depth dependence on η_{slab}/η_o and η_{lith}/η_o for models 1a–11c. The basin depth, indicated by the circle size, increases with increasing η_{slab}/η_o, but shows less dependence on η_{lith}/η_o or other viscosity variables.

DeBremaecker (1977), the forebulge forms in response to viscous flexure of the slab and lithosphere. When the slab is strongly coupled to the surface, the weight of the slab and flow in the mantle bend the lithosphere within the subduction zone. If the magnitude of the stress within the interior of the lithosphere is large enough, the overlying lithosphere is pushed up to form a forebulge outboard of the trench. In our models, forebulge heights consistent with observations (100–500 m) form when the lithosphere viscosity is relatively low ($<1000\ \eta_o$) and there is a strong lower mantle supporting part of the stress from the slab.

Velocity distribution

It is well known that the plate velocity within convection models depends strongly on the lithosphere viscosity. Stagnant lid convection occurs if the lithosphere viscosity is too high (e.g. Torrance & Turcotte 1971) or localized regions of weakness at plate boundaries are not included (Jacoby & Schmeling 1982). While the models discussed in this section do have a fault acting as a zone of weakness at the plate boundary, the velocity in the lithosphere is still strongly dependent on both the lithosphere and slab viscosity. Slab pull, from the negative buoyancy of the slab, is the force driving plate motion. In order for slab pull to be effective, the slab must be strongly coupled to the subducting, oceanic plate and the velocity of the plate will be comparable to the velocity of the slab. We find that for models with a large (100×) decrease in viscosity from the lithosphere to the slab, there is little flow in the lithosphere, even though flow in the slab can exceed 15 cm yr^{-1} for some models (Fig. 6). We quantify this effect by computing the plate mobility, M, which we define as

$$M = \frac{v_{lith}^{max}}{v_{slab}^{max}} \times 100, \qquad (13)$$

where a value of $M = 100$ indicates perfect coupling between the lithosphere plate and the slab. The maximum plate mobility found
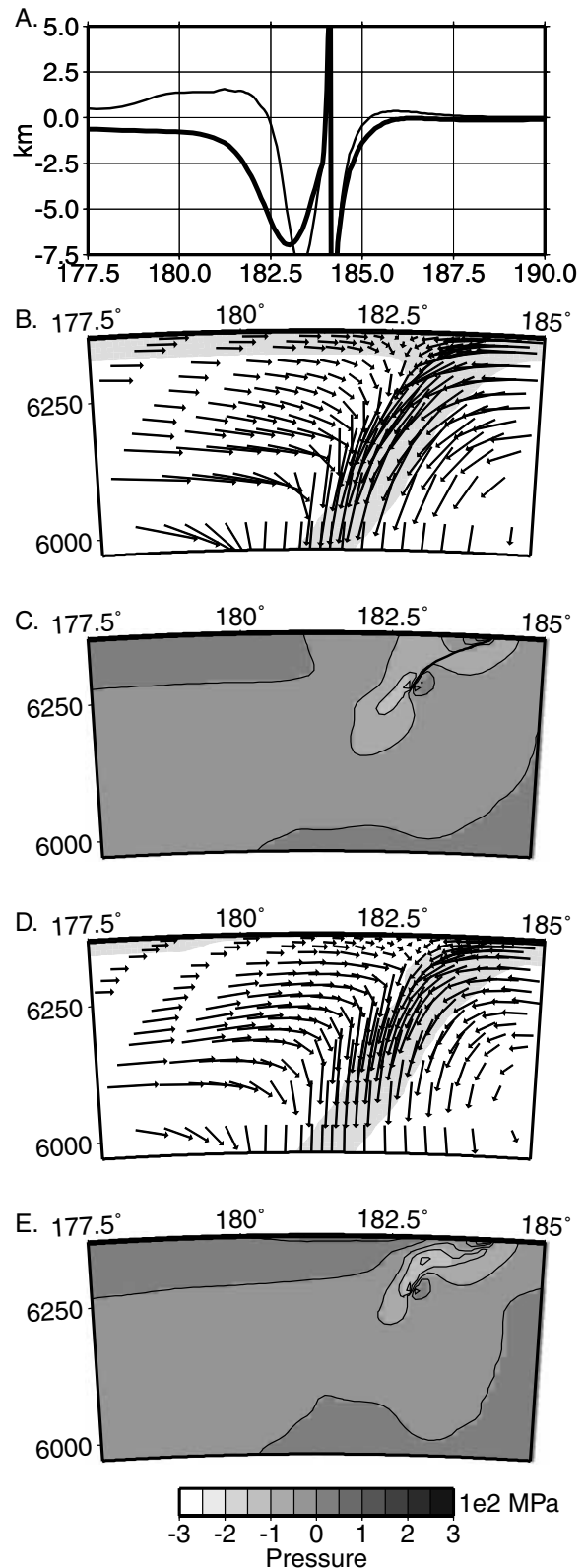
Figure 5. (a) Comparison of topography for models without (4b, thick) and with (4byl, thin) young lithosphere on the overriding plate. (b) and (c) Flow and pressure for model 4b, respectively. (d) and (e) flow and pressure for model 4byl, respectively. The grey scale for pressure is for (c) and (e) with a contour interval of 50 MPa. Location of the slab and lithosphere in (b) and (d) is indicated by the grey region ($T' < 0.5$). The maximum velocity is 2 cm yr^{-1}. See Table 2 for model parameters.
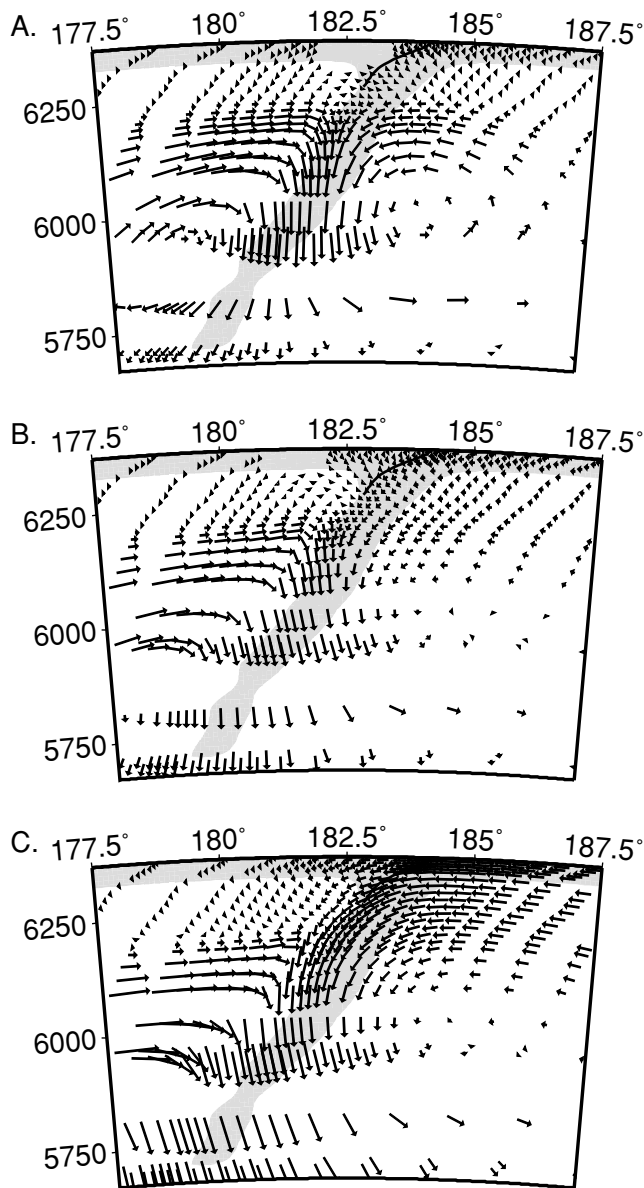
Figure 6. Velocity cross-sections for three models with equivalent viscosity structure except for the slab viscosity in the upper mantle. (a) Model 2b ($\eta_{slab} = 10\eta_o$), $v_{max} = 3.5$ cm yr^{-1}, $M = 6$. (b) Model 2c ($\eta_{slab} = 100\eta_o$), $v_{max} = 1.5$ cm yr^{-1}, $M = 21$. (c) Model 2d ($\eta_{slab} = 100\,\eta_o$), $v_{max} = 0.5$ cm yr^{-1}, $M = 49$. The velocity vectors in each cross-section are scaled by the maximum so that the flow distributions can be compared. The location of the slab is indicated by the grey region ($T' < 0.5$).

in our models is for model 7a ($M = 80$), in which the slab and lithosphere viscosities are both $100\eta_o$. This ratio may only reflect the relative viscosity of the slab and the lithosphere within the subduction zone if the plate is weakened as it nears the subduction zone. However, mobility decreases for models with higher lithosphere viscosity regardless of whether the slab and lithosphere viscosity are equal.

The viscosity of the slab also affects flow near the bottom of the slab. Models with a strong lower mantle ($100\eta_o$), and progressively stronger slabs, exhibit a rotation of the flow from slab-parallel to vertical flow (oblique to the dip of the slab) between 300 and 670 km (Fig. 6). In weak slab models (model 2b, Fig. 6a, $\eta_{slab} = 10\eta_o$) the upper portion of the slab simply flows (or falls) away from the

lithosphere in response to the negative buoyancy of the slab beneath. Near the bottom of the slab, the flow slows down and is deflected sideways by the increase in viscosity from the upper to the lower mantle. In model 2c (Fig. 6b, $\eta_{slab} = 100\eta_o$), the slab and lower-mantle viscosity are equal ($100\eta_o$), causing less deflection of the flow near the bottom of the slab. Stronger coupling between the slab and the lithosphere, and the increased viscosity of the slab, cause the slab to act as a stress guide to the surface. In this case, rather than falling away from the lithosphere, the shallow portion of the slab bends in response to the dense slab below. In model 2d ($\eta_{slab} = 1000\,\eta_o$, Fig. 6c) this stress guide effect increases as the slab is now stronger than the lower mantle and has the same viscosity as the lithosphere. In this case, there is no deflection or slowing of the flow within the slab in the transition zone and the bending of the strong slab acts as a boundary between the flow above and below the slab.

Slab strain rate and stress

Strain rates within the slab provide a direct constraint on the absolute viscosity of the slab. As discussed earlier, the minimum strain rate within the Tonga–Kermadec slab is estimated from the strain-rate release owing to deep seismicity (200–650 km), of 5×10^{-16} s^{-1}. We find that for models with $\eta_{slab}/\eta_o \geq 1000$, the average strain rate (volume-averaged second strain invariant) in the slab deeper than 100 km is less than 5×10^{-16} s^{-1}. Therefore, the viscosity of the slab must be less than approximately 3×10^{23} Pa s within the upper mantle to be consistent with the observed minimum strain rate from seismicity. This result is further verified by testing models at both higher and lower reference viscosity. Models 12 and 5c (Table 2) have the same absolute viscosity for the slab ($\eta_{slab} = 3 \times 10^{23}$ Pa s), but model 12 has a higher reference viscosity ($\eta_o = 3 \times 10^{21}$ Pa s) and a lower η_{slab}/η_o ratio ($100\times$) than model 5c ($1000\times$). However, both have approximately the same average strain rate in the slab ($\sim 1.8 \times 10^{-16}$ s^{-1}) and fail to meet the strain-rate constraint. Similarly, model 13 has a lower reference viscosity ($\eta_o = 3 \times 10^{19}$ Pa s) and higher η_{slab}/η_o ratio ($1000\times$) than model 4b ($100\times$), but both have the same slab viscosity (3×10^{22} Pa s) and the same slab strain rate ($\sim 8 \times 10^{-16}$ s^{-1}), meeting the strain-rate constraint.

In addition to the average strain rate within the slab, the distribution of the strain rate with depth depends on the viscosity of the slab. The observed distribution of strain-rate release from seismicity decreases with depth to 300 km, has a minimum from 300 to 400 km, and increases again below 400 km. This pattern is seen in models with weaker slabs ($\eta_{slab}/\eta_o = 1$–100). For models with stronger slabs, the minimum occurs between 400 and 500 km or there is no minimum. The average stress in the slab, $\bar{\sigma}$, defined as $\eta_{slab}\bar{\epsilon}$, also shows a systematic dependence on the slab viscosity, with only a slight dependence on other aspects of the viscosity structure (Table 2). Stress within the slab increases from a value of around 1 MPa for a very weak slab ($\eta_{slab}/\eta_o = 1$) to 100 MPa for a very strong slab ($\eta_{slab}/\eta_o = 10^4$). For a given slab viscosity, the stress within the slab varies by less than a factor of 2. This close dependence of slab stress on slab viscosity indicates that deformation of the slab is largely independent of the flow in the surrounding mantle, and the viscosity of the slab may be a better choice for the reference viscosity in mantle flow models driven by slab buoyancy.

Stress orientations

The orientation of stress within the slab is sensitive to both the viscosity of the slab and the change in viscosity from the upper to the lower mantle. Globally, stress orientation within slabs is observed to
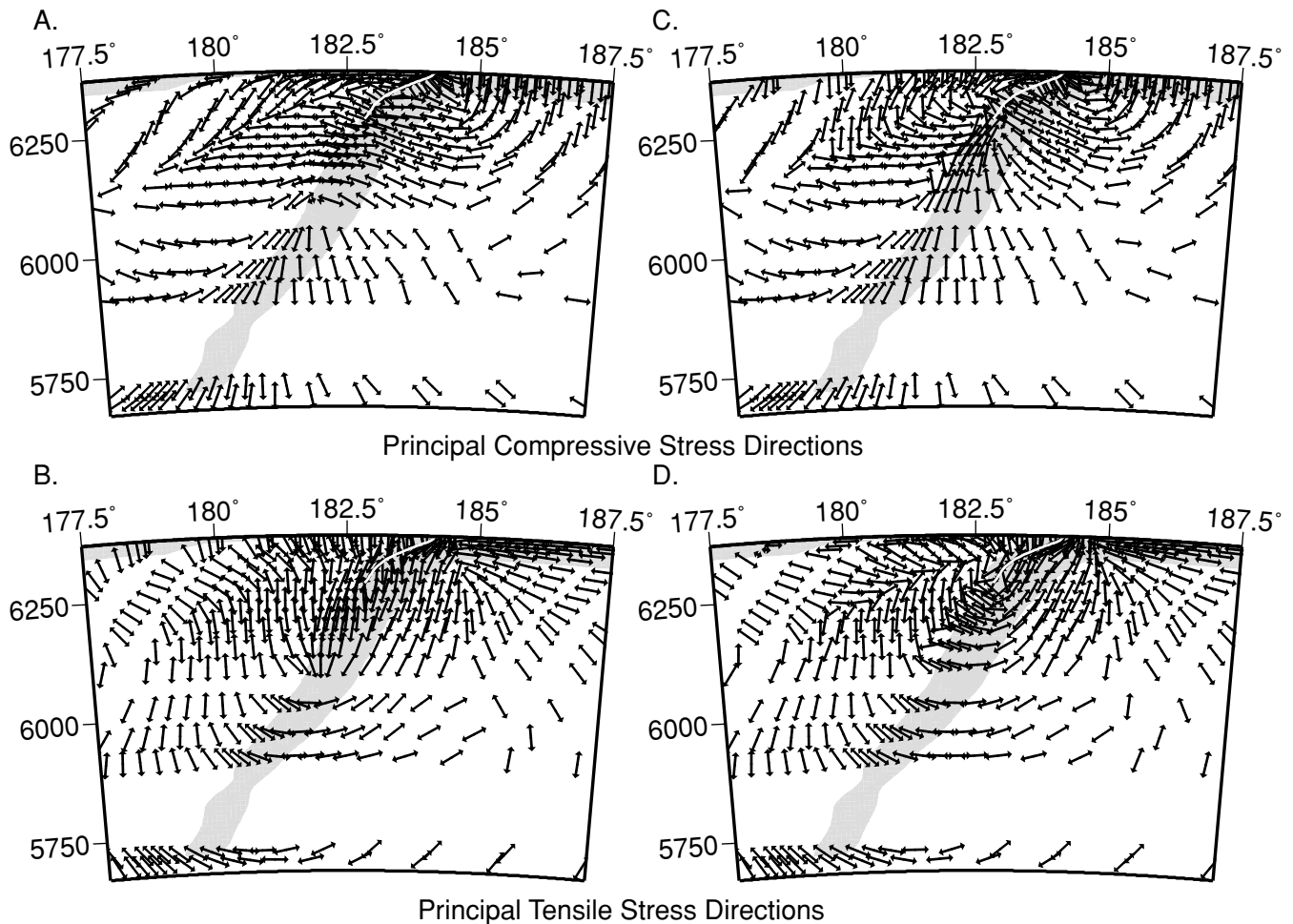
Figure 7. Principal stress directions: (a) and (b) are the principal compressive and tensile stress directions, respectively, for model 4byl. The slab is in down-dip tension from 100 to 350 km and down-dip compression below 350 km, while the overriding plate is in horizontal compression. (c) and (d) Same as (a) and (b) for model 4byl with a low-viscosity wedge (fw9). The slab is in down-dip compression from the base of the lithosphere to 670 km, and the overriding plate is in horizontal extension in a 400 km wide region beyond the fault-tip.

transit from down-dip tension to down-dip compression at around 300 km depth. We find this pattern in all models with a weaker slab ($\eta_{slab}/\eta_o = 1$–100) and strong lower mantle ($\eta_{lm}/\eta_o = 100$) (Figs 7a and b). This pattern is caused by the upper portion of the slab falling into the mantle and pulling the overlying mantle with it, creating vertical or down-dip tension in the shallow portion of the slab. Deeper in the slab, the resistance to flow at 670 km depth is transmitted up through the slab, putting the lower portion of the slab in compression. Strong slabs or slabs in models with a weaker lower mantle ($\eta_{lm}/\eta_o = 1$–10) are in down-dip tension throughout. In these cases, because the slab is stronger than the lower mantle, the resistance to flow is only felt by the leading edge of the slab and is not transmitted up through the slab. None of these models are able to fit the observations that some slabs may be in down-dip compression throughout (e.g. Tonga–Kermadec and Izu–Bonin).

Along the top surface of the subducting lithosphere, the stress orientation rotates from horizontal extension approaching the subduction zone to horizontal compression. The steep dip of the fault (see Section 5.4) causes flow within the subducting lithosphere to change from a horizontal flow direction to flow at 30°, parallel to the dip of the fault in the upper 10 km. This rapid change in flow near the fault creates a small region of compression in the subducting plate

seaward of the fault. These stress orientations are inconsistent with observations of extensive normal faulting of the subducting lithosphere within the trench, indicating that this region is in horizontal extension throughout (Lee & Powell 1982; Ogawa *et al.* 1997).

Young lithosphere

In the models discussed above, the lithosphere on the overriding and subducting plates is assumed to be of uniform thickness, determined by the age (50 Ma) of the plate. However, for some subduction zones, the upper plate contains a backarc spreading centre, with a young lithosphere immediately above the slab (e.g. the Tonga–Kermadec slab, is overlain by the Lau and Havre Trough spreading centres, with lithosphere less than 5 Myr). A younger lithosphere translates into a thinner strong, dense boundary layer above the slab and influences the basin topography above the slab in two ways. First, since the lithosphere is thinner, the topography is shallower as a result of isostatic compensation (by 1.5–2.5 km) (Fig. 5a). Secondly, the flow and pressure distributions above the slab are modified (Figs 5b–d). Flow in the wedge has a slight upward component of velocity entering the shallow portion of the wedge beneath the younger lithosphere. The region of low pressure above the slab becomes more

concentrated towards the fault and a region of higher pressure forms along the surface beneath most of the region with young crust. These changes lead to a narrower and slightly deeper basin, closer to the trench, with positive dynamic topography on the side of the basin furthest from the trench. In addition, a small forebulge develops in models that did not have a forebulge with uniform lithosphere age, or the forebulge height increases. This is caused by increased bending of the lithosphere in response to less viscous coupling between the shallow (50–100 km) portion of the wedge and the slab.

5.2 Low-viscosity wedge models

Understanding the dependence of topography, velocity and strain rate on radial- and temperature-dependent variations in viscosity in these basic 2-D models provides the background needed to investigate the role of strong lateral variations in viscosity owing to processes other than temperature variations. As discussed earlier, several lines of evidence (seismological, rock mechanics, geochemistry) suggest that the viscosity of the wedge may be several orders of magnitude less than the surrounding asthenosphere and mantle lithosphere. Billen & Gurnis (2001) present the first results showing that a low-viscosity wedge reduces the basin topography on the overriding plate, making it possible to better match the observed topography and the geoid. In the following section we expand upon that initial study by fully exploring low-viscosity regions of different shapes and viscosity, in models with different radial- and temperature-dependent viscosity structures.

Geometry of the wedge

As the distribution of low-velocity material in the wedge is not well constrained by seismological observations, we test several different shapes for this region. The geometry of the LVW, described by four parameters, $(d_{min}, d_{max}, w_b, w_t)$, is illustrated in Fig. 8. These four parameters describe two types of regions: full wedge (fw), for models with w_b and w_t greater than 100 km, and slab parallel (sp), for models with w_b and w_t less than 50 km (Fig. 8). A full list of the 16 different wedge shapes tested is given in Table 3. The influence of the LVW shape on topography and distribution of flow in the wedge is first discussed for the background model 4byl. A subset

surface
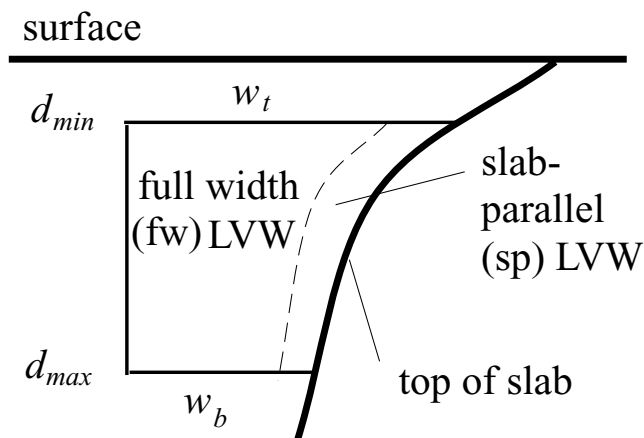
Figure 8. Geometry of the low-viscosity wedge. d_{min} is the minimum depth to the top of LVW, d_{max} is the maximum depth to the bottom of LVW, w_b is the width of the base of LVW from the top of the slab, and w_t is the width of the top of LVW from the top of the slab.

Table 3. Models with an LVW for various background viscosity structures (see Table 2) and wedge viscosity: geometry (d_{min}, d_{max}, w_t and w_b defined in Fig. 8), basin depth (h_{basin}), change in basin depth compared with model with no LVW (Δh_{basin}), and mobility, (M). A- Viscosity model 4byl, $\eta_{lvw} = 3 \times 10^{19}$ Pa s. B- Viscosity model 5byl, $\eta_{lvw} = 3 \times 10^{19}$ Pa s. C- Viscosity model 6cyl, $\eta_{lvw} = 3 \times 10^{19}$ Pa s. D- Viscosity model 5byl, $\eta_{lvw} = 3 \times 10^{18}$ Pa s. E- Viscosity model 5byl, $\eta_{lvw} = 3 \times 10^{17}$ Pa s.

Model	d_{min}	d_{max}	w_b	w_t	h_{basin} (km)	Δh_{basin}	M
			2-D low-viscosity wedge models				
A-fw1	20	100	200	270	−2.35	5.81	98
A-fw2	20	100	100	170	−2.26	5.90	98
A-fw3	50	100	200	250	−3.74	4.42	97
A-fw4	50	100	100	150	−3.72	4.44	97
A-fw5	20	200	200	350	−2.35	5.81	97
A-fw6	20	200	100	250	−2.31	5.85	97
A-fw7	50	200	200	320	−3.51	4.65	97
A-fw8	50	200	100	220	−3.59	4.57	96
A-fw9	20	300	200	400	−2.36	5.80	97
A-fw10	20	300	100	300	−2.31	5.85	96
A-fw11	50	300	200	370	−3.58	4.58	95
A-fw12	50	300	100	270	−3.57	4.59	95
A-sp1	20	200	50	50	−1.94	6.22	96
A-sp2	20	200	50	50	−3.51	4.65	96
A-sp3	50	300	50	50	−1.95	6.21	96
A-sp4	50	300	50	50	−3.57	4.59	95
A-sz1a	0	120	40	40	−5.32	2.84	93
A-sz2a	0	120	40	40	−3.54	4.62	96
B-fw1	20	100	200	270	−5.39	6.20	89
B-fw5	20	200	200	350	−5.44	6.15	89
B-fw9	20	300	200	400	−4.94	6.65	90
B-sp1	20	200	50	50	−5.12	6.47	88
B-sz1a	0	120	40	40	−7.05	4.54	66
B-sz2a	0	120	40	40	−6.55	5.04	70
C-fw1	20	100	200	270	−6.54	14.24	97
C-fw5	20	200	200	350	−6.32	14.46	100
C-fw9	20	300	200	400	−6.30	14.48	100
C-sp1	20	200	50	50	−6.42	14.36	96
D-fw1	20	100	200	270	−5.33	6.26	90
D-fw5	20	200	200	350	−5.58	6.01	90
D-fw9	20	300	200	400	−5.43	6.16	90
D-sp1	20	200	50	50	−5.14	6.45	88
D-sz1b	0	120	40	40	−6.72	4.87	79
D-sz2b	0	120	40	40	−4.47	7.12	83
E-fw1	20	100	200	270	−5.59	6.00	88
E-fw5	20	200	200	350	−5.63	5.96	90
E-fw9	20	300	200	400	−5.43	6.16	90
E-sp1	20	200	50	50	−5.14	6.45	88
E-sz2c	0	120	40	40	−4.06	7.53	87

of the wedge shapes is further investigated for background models 5byl and 6cyl (Table 3).

Topography

Previous studies have found that the influence of the LVW on basin topography depends strongly on the minimum depth of the LVW (Billen & Gurnis 2001). For all 16 wedge shapes investigated, models with a minimum depth of 20 km reduce the basin depth by 6 km, while models with a minimum depth of 50 km only reduce the basin depth by 4 km. This is also true for the slab parallel LVW, which extends only 50 km from the top of the slab. This result differs from previous results, which found that a wide LVW was necessary to reduce the basin topography over the full width of the basin. However, these two results are consistent and the difference is a result of the age of the overriding plate.

© 2003 RAS, *GJI*, **153**, 359–388

In previous models, the overriding plate had a uniform age, and therefore, uniform thickness and density (Billen & Gurnis 2001). In these models, a wide (200 km) and shallow ($d_{min} = 20$ km) low-viscosity region was necessary to decrease the basin depth over the full width of the basin. If a narrower LVW was used, the basin depth was only reduced in the region above the LVW and increased beyond the LVW. As presented in the previous section, including young lithosphere on the overriding plate narrows the basin towards the trench and creates positive topography on the side of the basin furthest from the trench. The change in the geometry of the wedge caused by bringing lower-viscosity asthenosphere into the shallow portion of the wedge beneath the young lithosphere has a similar effect as the LVW in the previous models. However, because the decrease in viscosity is only between the mantle lithosphere and the shallow portion of the wedge, the flow and pressure within the wedge are only modified slightly, and therefore the basin only becomes narrower, not shallower. Both young lithosphere and, at least a narrow low-viscosity region, are necessary to eliminate the deep basin on the overriding plate.

The change in the shape of the low-pressure region above the slab caused by introducing the LVW also increases the trench depth and leads to a forebulge on the subducting plate. The forebulge develops because the viscosity of the region above the slab decreases, reducing coupling of the slab buoyancy to the wedge, and causing higher stresses to be transmitted to the lithosphere.

As with the other viscosity parameters, it is important to determine whether the relative viscosity between the LVW and the slab or lithosphere influence the ability of the LVW to reduce the basin topography. For models without an LVW, the basin depth depends strongly on the slab viscosity. However, the LVW has the same effect on topography for models with a strong slab as it does for models with a weaker slab. Similarly, the topography is reduced by the same amount for models with $\eta_{lvw} = 3 \times 10^{19}$ Pa s as for models with $\eta_{lvw} = 3 \times 10^{17}$ Pa s (compare model sets B, D and E). Therefore, neither the relative viscosity between the slab and the LVW, or the lithosphere and LVW, control the change in dynamic topography. Instead, the modification of the geometry owing to the initial small change of the wedge viscosity has the largest effect on the topography.

Wedge flow

While topography in models with a young lithosphere and LVW depends only on the minimum depth of the LVW, and not the width or depth extent, the flow distribution in the wedge does depend on both the shape of the LVW and its viscosity. The shape of the wedge changes the pressure field above the slab. Instead of low pressure extending from the slab to the surface, the low-pressure region is focused within the low-viscosity region and a high-pressure region forms above the LVW. However, the magnitude of the pressure above the slab is determined by the density anomaly and the viscosity of the slab. Therefore, further reducing the viscosity of the LVW does not change the magnitude of the pressure. Instead the flow velocity increases, since there is less viscous resistance, and the same driving force is transmitted to the wedge (see Appendix D).

In addition to higher velocities in the wedge, the LVW increases the plate mobility. For models 4byl, 5byl and 6cyl, the plate mobility increases to ∼98 in the presence of LVW with $\eta_{lvw}/\eta_o = 0.1$. While the magnitude of velocity in the wedge continues to increase with decreasing wedge viscosity, only a modest increase in velocity of the slab occurs ($1.5\times$) and is the same regardless of further decreasing the wedge viscosity. This is consistent with the strain rate and stress results for models without an LVW, which have only a strong dependence on the slab viscosity.

Stress orientations

As mentioned earlier, the Tonga–Kermadec slab (and sections along strike of other slabs) appears to be in down-dip compression at all depths. An important result of including a low-viscosity region in the wedge is that the orientation of the principal stress axis in the shallow portion of the slab is in down-dip compression along the top half of the slab (Figs 7c and d). This is the first time this aspect of the stress orientation within a slab has been reproduced in a dynamic model. The change in stress orientation within the slab is caused by the change in coupling to the overlying wedge mantle. Without the LVW, the shallow portion of the slab is partially supported by viscous stresses, from strong coupling of the wedge flow to the downward flow of the slab, causing down-dip extension. This support of the slab from the material above is greater than the compressional stresses transmitted up through the slab, so the top portion of the slab is in extension, while the lower portion of the slab is in compression. The LVW reduces the support of the slab from above, causing the shallow part of the slab to decouple from the larger-scale flow and to behave more as a viscous plate bending in response to the load of the slab beneath.

The orientation of principal stress directions in viscous bending (flexure) depends not on the curvature of the strong slab (as in elastic flexure), but on the direction in which the curvature is changing (Houseman & Gubbins 1997). For example, the compressional stress direction in viscous flexure aligns parallel to a surface becoming less convex (unbending) and perpendicular to a surface becoming more convex (bending). Therefore, it would be expected that, as the surface of the lithosphere changes from strongly convex in the upper 100 km of the slab to less convex between 100 and 300 km, the orientation of the principal compressive stress axis would rotate from perpendicular to the slab surface to parallel to the slab surface. Therefore, the LVW decouples the slab from the overlying wedge, allowing it to deform as a bending viscous plate independent of flow in the wedge.

The LVW also modifies the orientation of stress within the overriding plate above the wedge. In models without an LVW, the overriding plate is in horizontal compression, while models with an LVW are in horizontal extension in a region approximately 400 km wide beginning 150 km from the trench (Fig. 7). Including a region of low density within the wedge (see Section 5.3), broadens this region of extension, in particular for cases with a reversal of flow along the boundary of the LVW furthest from the slab.

5.3 Buoyancy in the LVW

If the low-viscosity region within the wedge is caused by melt or alteration of the mineralogy owing to the presence of water, then it is probable that the LVW will also have a lower density than the surrounding mantle. Models with density anomalies of -10 and -20 kg m^{-3} are investigated for four wedge geometries: fw1, fw5, fw9 and sp1 (Table 4). The smaller density anomaly leads to only a maximum 0.72 km increase in topography on the overriding plate for the largest LVW (fw9). The larger-density anomaly leads to an increase in topography of up to 1.65 km, although the basin depth close to the trench only decreases slightly.

The positive buoyancy in the LVW has a strong influence on the flow in the wedge, creating a large upward component of flow in the smaller, full width (fw1 and fw5) wedge models and a reversal

Table 4. Models with a low-viscosity and low-density wedge for LVWs of various shapes (see Table 3) and the background viscosity structure: Density anomaly ($\delta\rho$), basin depth (h_{basin}), change in backarc height ($\Delta h_{backarc}$), and mobility (M). (a) Viscosity model 4byl, $\eta_{lvw} = 3 \times 10^{19}$ Pa s. (b) Viscosity model 5byl, $\eta_{lvw} = 3 \times 10^{19}$ Pa s.

Model	LVW Model	$\delta\rho$ (kg m^{-3})	h_{basin}	$\Delta h_{backarc}$	M
		2-D LVW models with positive buoyancy			
A-bw1a	fw1	−10	−1.79	0.29	98
A-bw1b	fw1	−20	−1.58	0.64	99
A-bw2a	fw5	−10	−1.86	0.52	98
A-bw2b	fw5	−20	−1.84	1.19	99
A-bw3a	fw9	−10	−2.05	0.71	98
A-bw3b	fw9	−20	−0.08	1.65	100
A-bw4a	sp1	−10	−1.34	0.02	98
A-bw4b	sp1	−20	−1.31	0.06	98
B-bw5a	fw1	−10	−4.62	0.31	87
B-bw5b	fw1	−20	−4.49	0.66	89
B-bw6a	fw5	−10	−4.44	0.57	91
B-bw6b	fw5	−20	−3.78	1.07	95
B-bw7a	fw9	−10	−4.26	0.72	93
B-bw7b	fw9	−20	−3.43	1.61	100
B-bw8a	sp1	−10	−4.21	0.07	87
B-bw8b	sp1	−20	−4.17	0.13	87
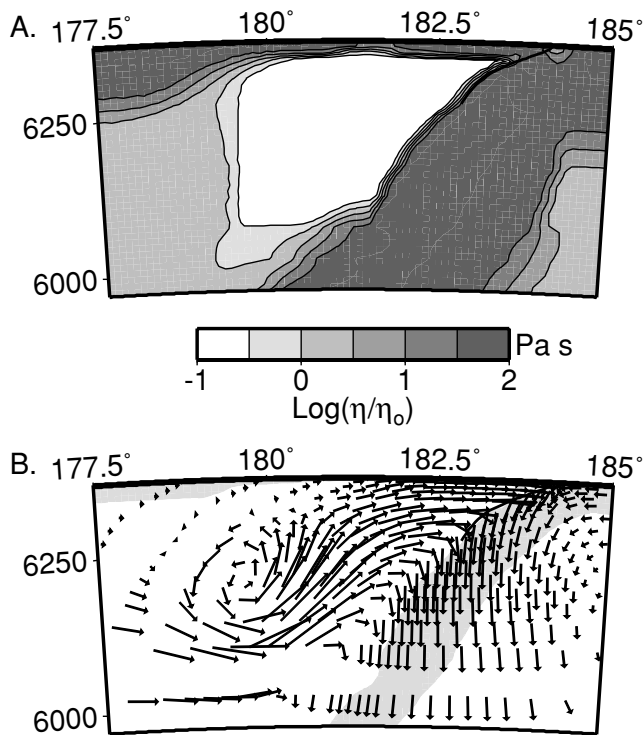
Figure 9. (a) Viscosity model (the contour interval is 0.5) and (b) flow for model 4byl with an LVW including a density anomaly of −20 kg m^{-3}. A reversal of flow occurs near the boundary of the LVW furthest from the slab. The slab location is indicated by the shaded region ($T' < 0.5$).

of flow in the large (fw9) LVW model with a −20 kg m^{-3} density anomaly (Fig. 9). Davies & Stevenson (1992) find a similar reversal of flow using kinematic models with superimposed flow of a small buoyant low-viscosity region. They were able to achieve flow reversals with smaller buoyant regions using a much lower viscosity in the surrounding asthenosphere (3×10^{17} Pa s). They also found that the reversal of flow depended on the integrated buoyancy, i.e.

there is a trade-off between the volume of buoyant material and the density anomaly. This explains why we only see flow reversal for the largest LVW and no noticeable change in flow for the slab parallel wedge.

5.4 Fault singularity

The presence of a dipping fault is required to create both asymmetric flow at the surface and trench morphology similar to observations (Zhong & Gurnis 1992; Zhong & Gurnis 1994; Zhong *et al.* 1998). However, the fault also introduces a stress singularity into the model that leads to an unconstrained trench depth on the subducting plate, and forearc height on the overriding plate. The magnitude of the stress singularity increases as the mesh size decreases. Therefore, in our models, which have element sizes of the order of 2.5 km, much smaller than used in previous models (Zhong *et al.* 1998), this stress singularity leads to unreasonable trench depths and forearc heights. Another source contributing to the excessively deep trenches may be the dip of the fault used in our models. The fault dip at the surface for most subduction zones ranges from 10° to 20°. In our models, a fault dip of less than 30° leads to numerical errors owing to distortion of the rectangular elements.

Stress at the fault can be constrained by reducing the viscosity around the fault, either by creating a weak zone surrounding the fault or using a yield stress. Physically this is justified because rock has a finite strength, and if the stress is higher than this value, the rock yields, limiting the maximum stress to the strength of the rock (elastic–plastic rheology) (Kohlstedt *et al.* 1995). Both a yield stress and a narrow shear zone around the fault with a viscosity reduction of 0.1–1η_o (for $\eta_{lith} = 100\eta_o$ a yield stress of 75 MPa is used to focus the reduction in viscosity along the fault) decrease the trench topography to ∼4–5 km and the forearc high to less than 1 km. However, both of these methods lead to broadening of the trench by a factor of 2–3, where the deepest portion of the trench is shifted seaward up to 50 km from the fault tip, and the trench profile of the subducting plate within the trench changes from convex downwards to concave downwards. This change in morphology is caused by the width of the shear zone or yielded area, which usually includes four to ten elements (8–22.5 km) on each side of the fault. This number of elements is needed because the drop in viscosity across a single element must be less than a factor of 3 for numerical accuracy. Therefore, while the trench topography and forearc high are greatly reduced, use of a yield stress or shear zone is not a satisfactory method for constraining the stress singularity at the fault tip.

5.5 Summary of 2-D models

The large set of 2-D models explored illustrates the sensitivity of different observations to various aspects of the viscosity structure and provides constraints on the range and type of viscosity variations consistent with these observations. The main conclusions from these models are as follows.

(1) The maximum viscosity of the slab is less than 3×10^{23} Pa s, based on observations of strain rates, stress orientations and plate mobility.

(2) Weakening of the slab relative to the subducting plate should be less than a factor of 100 for effective coupling.

(3) Lithospheric thickness variations arising from plate age can modify flow in the wedge and dynamic topography if a young backarc spreading centre is present above the slab.

(4) A low-viscosity region in the wedge greatly reduces basin topography on the overriding plate, changes the orientation of stress

in the shallow portion of the slab from down-dip tension to down-dip compression, and creates a region of horizontal extension within the overriding plate.

(5) A large buoyant region in the wedge can cause a reversal of flow in the wedge, contributes to the dynamic topography and broadens the region of extension on the overriding plate.

Based on these conclusions and results from previous modelling discussed in Section 2, we define a preferred viscosity structure. This viscosity structure includes a strong lower mantle ($\eta_{lm}/\eta_o = 100$), a small increase in viscosity in the transition zone ($\eta_{tran}/\eta_o = 10$), a weak slab ($\eta_{slab}/\eta_o = 10$) and a small increase in lithosphere viscosity relative to the slab ($\eta_{lith}/\eta_{slab} = 10$) and a low-viscosity region in the wedge. Our choice of a weak slab and lithosphere viscosity is based on mobility constraints and the dependence of the basin depth on the slab viscosity and probably only reflects what this ratio is within the subduction zone. The exact size, shape and minimum viscosity of the low-viscosity region in the wedge are not constrained by these generic 2-D models.

6 3-D MODELS OF THE TONGA–KERMADEC SUBDUCTION ZONE

We begin our study of the 3-D dynamic flow in the Tonga–Kermadec subduction zone using the preferred viscosity structure described above, excluding the low-viscosity region (model 1). In addition to the constraints provided by topography, strain rates and stress orientations, we now include the geoid as a further constraint on the 3-D viscosity structure. Although we know from the 2-D results that this basic model will not match the observed topography, this model provides a reference as we add complexities to the viscosity and density structure. 11 3-D models of the Tonga–Kermadec region are presented with cross-sections of dynamic topography in Fig. 10 and maps of dynamic topography and geoid in Figs 11 and 12, for selected models. Table 5 lists each 3-D model, with a description of the modifications to the viscosity or density structure. In addition to the influence of the shallow viscosity and density structure, we also investigate the sensitivity of the predicted geoid to the deeper-density structure of the slab using models that extend the slab density into the lower mantle (model 9) or along the 670 km discontinuity (model 10) (see Section 6.4).

For each of the 3-D models we discuss the influence of the viscosity and density structure on the dynamic topography, stress orientation and geoid. In particular, we discuss the influence of dynamic topography on the predicted geoid (Section 6.1) The predicted geoid is then compared with the observed geoid (Section 6.4) using a spatio-spectral localization method (Simons 1996). This method enables us to compare geoid results from our regional models with the observed geoid without aliasing the long wavelengths owing to truncation of the observed field spatially or spectrally. It is important to note that while slabs other than the Tonga–Kermadec slab are present within the region of the 3-D models, these slabs are not included in the models. Therefore, we focus our attention on the region within 1500 km of the Tonga–Kermadec Trench, knowing that this will limit our ability to compare with observations at longer wavelengths.

6.1 Dynamic topography

The observed topography in the region of the Tonga–Kermadec subduction zone (Fig. 2) is characterized by a narrow, deep trench and
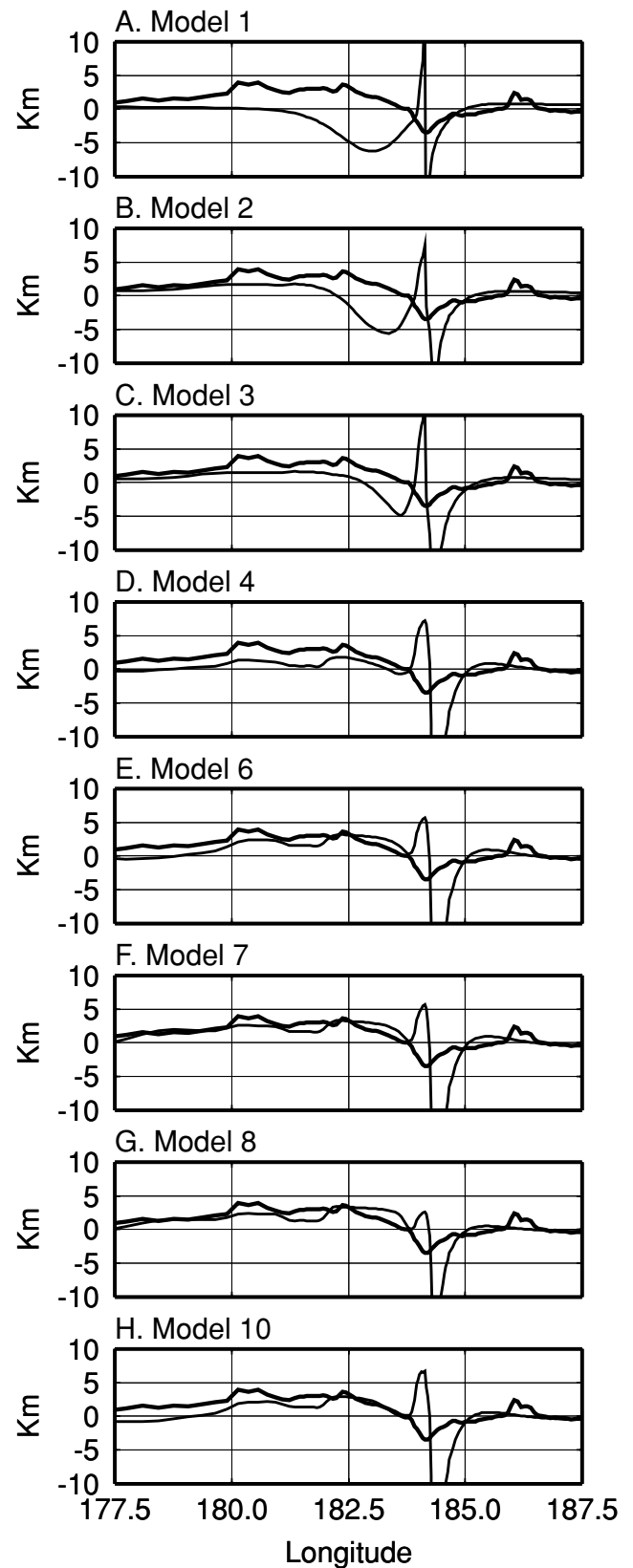
Figure 10. Cross-sections of topography for 3-D models 1–4, 6–8, and 10 at 28°S. Observed topography (thick line) shifted up by 3.5 km for comparison with the predicted topography (thin line). Model parameters are listed in Table 5.
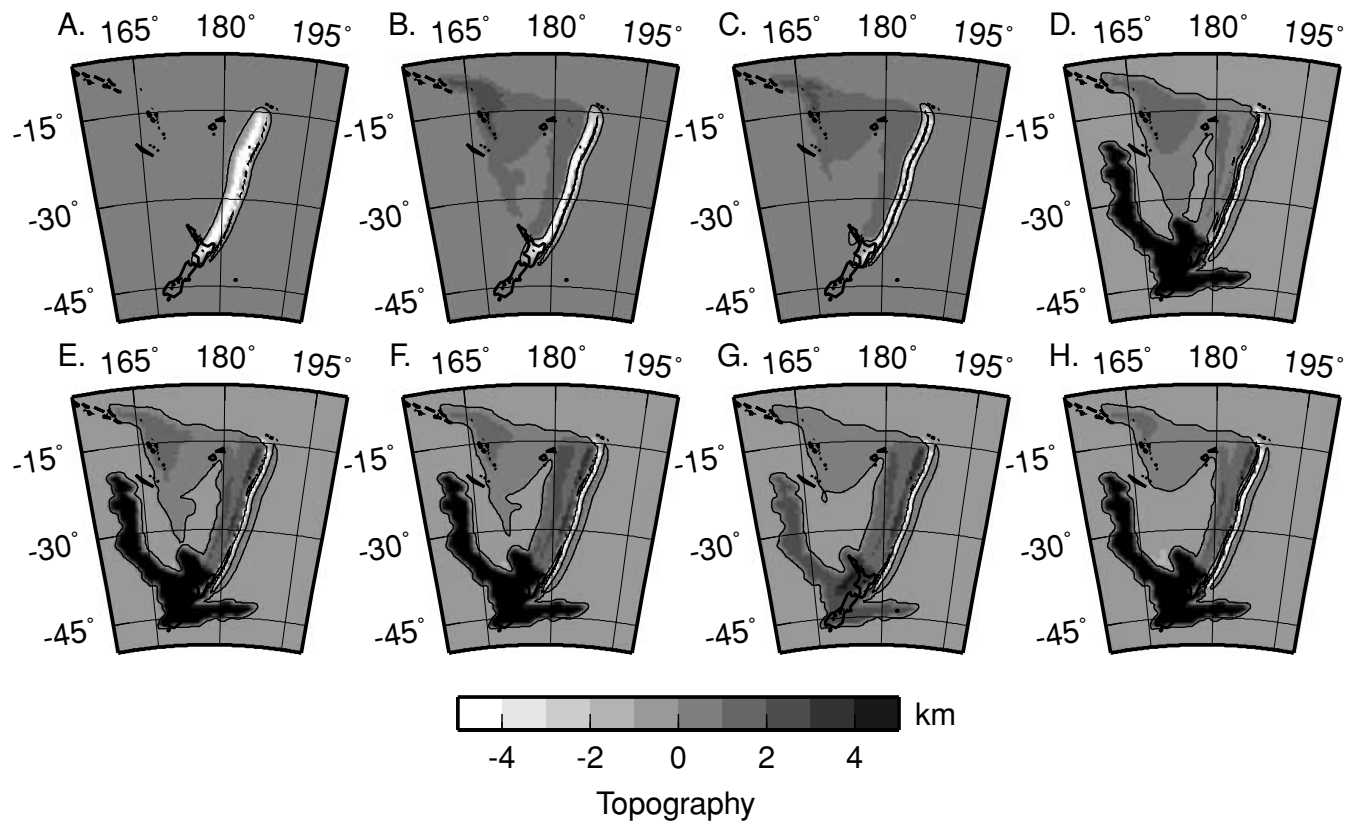
Figure 11. Maps of predicted topography for 3-D models. (a)–(d) models 1–4, (e)–(g) models 6–8, (h) model 10. See text for full discussion. Note that any variations in lithosphere age or crustal thickness within 300 km from the boundary domain are removed and set to an average background value for the ages (80 Ma) or zero for crustal thickness.
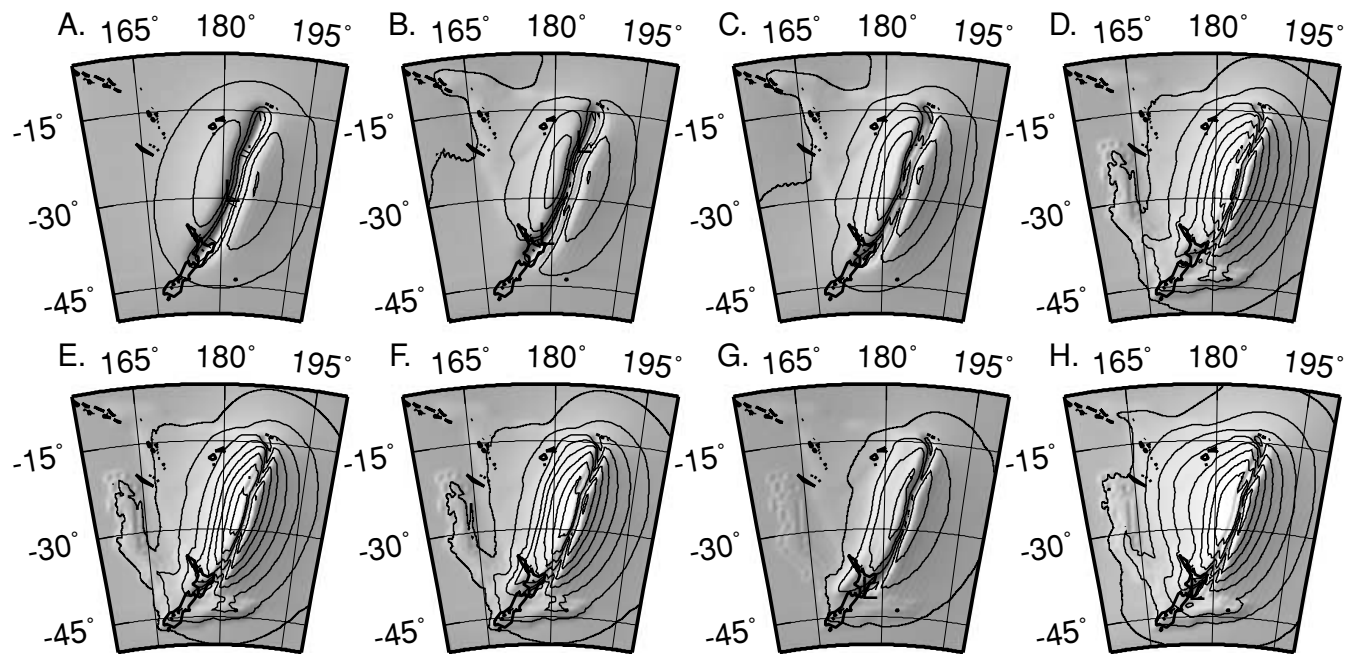
Figure 12. Maps of the predicted geoid for 3-D models. (a)–(d) models 1–4, (e)–(g) models 6–8, (h) model 10. The predicted geoid is everywhere positive in these models. A local minimum is observed over the backarc region of trench, depending on the model. The contour interval is 10 m. Note that because the fault singularity leads to unrealistically deep trenches, the maximum depth of the trench is limited to 5 km when calculating the geoid.

Table 5. Radial and temperature-dependent background viscosity structure is the preferred structure defined in Section 5.5 and is the same for all models ($\eta_{lm}/\eta_o = 100$, $\eta_{\text{tran}}/\eta_o = 10$, $\eta_{\text{slab}}/\eta_o = 100$, $\eta_{\text{lith}}/\eta_{\text{slab}} = 1$). The crustal density anomaly in models 3–11 is 300 kg m^{-3} with crustal thickness 9, 18 and 28 km for the Coleville ridge, Tonga–Tofua Arc and continents. In models 8 and 11, the thickness of the continental crust is reduced to 20 km to better match the observed topography.

Model	Viscosity structure	Density structure
		3-D models
1	No LVW	Uniform thickness lithosphere
2	No LVW	Lithosphere thickness from plate ages
3	LVW, fw5	Same as model 2
4	Same as 3	Add crustal density anomalies
5	Same as 3	Add low density in LVW, $\Delta\rho = -10$ kg m^{-3}
6	Same as 3	Add low density in LVW, $\Delta\rho = -20$ kg m^{-3}
7	Same as 3	Extend low-density region an additional 500 km west, $\Delta\rho = -20$ kg m^{-3}
8	Same as 3	Same as 7 with a decrease slab density by factor of 1.3 and a thinner continental crustal thickness (see caption).
9	Same as 3	Same as 4 with slab thermal anomaly extended to 1000 km depth.
10	Same as 3	Same as 4 with slab thermal anomaly extended 1000 km to the west along the 670 km discontinuity.
11	Same as 3	Same as 7 with a low-density region for basalt and harzburgite crust in the subducting slab extending down to 150 km.

a nearly 3 km difference in average depth between abyssal depths of the subducting Pacific Plate (4–5 km) and shallow bathymetry (2–3 km) of the overriding Australian Plate and backarc spreading system. Dynamic topography in models 1–3 display the same behaviour described for the 2-D models. Model 1, with only radial- and temperature-dependent viscosity variations, has a broad (300 km), deep (6 km) basin on the overriding plate, which clearly disagrees with the observed shallow bathymetry. In model 2, we include the observed age variation of the lithosphere (see Section 4.2). Including these age variations narrows the basin but does not greatly improve the fit to observed bathymetry near the trench.

Model 3 includes a low-viscosity region in the wedge along the entire length of the slab, with dimensions perpendicular to the trench given by the 2-D low-viscosity wedge shape, fw5 ($d_{\min} = 20$ km, $d_{\max} = 200$ km, $w_b = 200$ and $w_t = 350$ km). The basin is substantially reduced and the cross-section (Fig. 10c) shows that the long-wavelength profile of topography across the trench is similar to the observed. However, the low region on the overriding plate is still 5 km deep. The basin on the overriding plate is completely eliminated in model 4, which includes crustal thickness variations owing to the remnant and active island arc and continental crust to the southwest. Other crustal thickness variations exist within the model domain (mainly to the west of the south Fiji Basin), but are not included because they are far from the Tonga–Kermadec Trench. A narrow shear zone is included along the top surface of the fault. By limiting the shear zone to the overriding plate, we are able to decrease the height of the forearc without increasing the width of the trench. Including the crustal anomalies and shear zone improves the agreement with the observed bathymetry at short wavelengths. However, there is still a 1–1.5 km offset in the average depth on the overriding plate.

In the 2-D models, we found that decreasing the minimum viscosity of the wedge does not further decrease the basin depth. Therefore,

in models 5 and 6 we include regions of low-density material co-incident with the LVW in an attempt to better match the average depth of the overriding plate. The density anomaly in model 5 is -10 kg m^{-3} and in model 6 is -20 kg m^{-3}. The larger-density difference in model 6 provides a good match to the average depth on the overriding plate in the region above the LVW (Fig. 10e). However, the predicted topography decreases to the west, while the observed topography remains shallow.

In model 7 we extend the low-density region further west by an additional 500 km. This improves agreement with the observed bathymetry and suggests that lower-density material may exist in the shallow mantle throughout the region of past subduction extending to the New Caledonia basin (Kroenke 1984). Model 8 is identical to model 7 except that the slab density is reduced by a factor of 1.3. This change in slab density is achieved using a reduced coefficient of thermal expansion. However, the magnitude of all other density anomalies (crustal, wedge) are kept the same as in model 7. Despite this large change in the driving force from the slab, the topography is only modified within 50 km of the trench. Similarly, in models 9 and 10, there is no change in the topography, when the slab is extended into the lower mantle or along the upper–lower-mantle boundary. In model 11, which includes a density anomaly arising from basaltic crust within the subducting slab down to 150 km, there is a slight increase in topography, as this low-density region resists subduction. These models will be discussed further with respect to how these changes in density affect the fit to the geoid.

6.2 Geoid

The importance of dynamic topography on the geoid is illustrated by the maps of predicted geoid in Fig. 12. The deep basin in models 1–3 creates a broad (500 km) geoid low centred over the backarc region with an amplitude of 10–30 m. This geoid low narrows and shifts towards the trench in model 3 (with an LVW). The predicted long-wavelength geoid is positive with an amplitude of 40–60 m. In models 4–11 the shallow density anomaly within the LVW creates positive dynamic topography that is not completely compensated by the density anomaly. This leads to a much larger positive geoid at wavelengths of 500–1000 km, with amplitudes exceeding 100 m. In these models, the trench is marked by a small, short-wavelength geoid low of 10–20 m.

In model 8, the amplitude of the intermediate-wavelength geoid (500 km) is reduced by almost 40 m, although the pattern remains the same as in model 7. The difference between the predicted geoid for models 7 and 8, which have almost identical topography, demonstrates the importance of using both the dynamic topography and geoid to constrain the viscosity and density distribution. The effect of the low-viscosity region is to decouple the slab from the surface, rendering the topography insensitive to the buoyancy of the slab, while the geoid is still sensitive to both the driving force and the dynamic topography. We will return to this point in the discussion.

Finally, in model 10, extending the density anomaly of the slab west 1000 km within the transition zone increases the long-wavelength geoid by 20–30 m over the North and South Fiji Basins west of the trench, while above the trench the geoid only increases by 15 m. Since the predicted topography is not affected much by these deeper-density anomalies owing to decoupling of the flow from the surface by the LVW, the amplitude of the geoid arising from these deeper anomalies depends mainly on the magnitude of the density anomalies. Therefore, if the density of the slab in model 10 were also reduced by a factor of 1.3, as in model 8, we

would expect the long-wavelength geoid to decrease by this same factor.

6.3 Stress orientation in 3-D models

The choice of radial- and temperature-dependent viscosity structure ensures that the minimum strain rate within the slab in our models is at least as large as the observed strain-rate release from seismicity and that the minimum in strain-rate release occurs between 300 and 400 km depth (see Section 2.3). For 3-D models without an LVW (models 1 and 2), the stress pattern is the same as found in the 2-D models (compression in overriding plate and down-dip extension throughout most of the slab), with some along-axis compression in the shallow portion of the slab. The LVW in the 3-D models creates a more complex stress pattern within the shallow portion of the slab, which more closely agrees with observations (down-dip compression at all depths). The orientation of stress in the slab in the models is down-dip compression along the top portion of the slab deeper than 300 km (Fig. 13). However, between 100 and 200 km depth, the principal compression axes are oriented $20°–30°$ shallower than the dip of the slab. In addition, while the principal compression axes are aligned perpendicular to the local strike of the slab (approximately $10°$ north of west), the principal tension axes include a component of along-axis deformation. Therefore, the 3-D geometry of the slab affects the orientation of stress within the shallow portion of the slab. This result is not surprising, given the along-strike variation in the shape and depth extent of the slab, and the conclusion from the 2-D models that including an LVW allows stresses caused by viscous flexure within the slab to control the deformation of the slab.

In the 2-D models, we found that introducing a low-viscosity wedge caused the overriding plate to go into extension. For the 3-D models, only model 8 with a large, low-viscosity and low-density wedge and a lower-density slab, includes robust extension in the overriding plate. Instead, there is a transition from strongly compressional stresses in the overriding plate, for models without an LVW (models 1 and 2), to models with weaker compressional stresses and along-axis deformation, for models with a low-viscosity and low-density wedge (models 3–11).

### 6.4 Multiscale analysis of the geoid

The observed geoid over the Tonga–Kermadec region includes a very long-wavelength signal not included in our models (Fig. 1). This makes it difficult to compare the results of our models with the observed geoid directly. Instead, we use a spatio-spectral localization method to quantify the fit of the predicted geoid to the observed geoid as a function of position and wavelength (Simons 1996; Simons *et al.* 1997). Simons (1996) showed that a comparison between fields represented by a finite sum of spherical harmonics should take into account the spatial distribution of the source of the fields. If the sum is truncated, a spurious signal may exist on regions of the sphere not spatially correlated with the source of the signal. The localized amplitude of the observed geoid is shown in Fig. 14 as a function of position and wavelength, along an east–west profile at $28°S$. The rms amplitude reflects where the geoid has a large signal (power). In this cross-section it is clear that the observed geoid has a large signal at long wavelengths across the whole model domain, but only has a large signal at short wavelengths in the vicinity of the Tonga–Kermadec Trench ($185°$) in this cross-section.

The localization method, a form of multiresolution analysis, is similar to wavelet analysis. The filtering window in the spatial domain is a spherical cap with a characteristic spatial extent equal to twice the wavelength being considered. This choice of window balances the need for localization in both position and wavelength. Using this method we can calculate the localized rms amplitude of the observed and predicted geoid to assess what position and wavelengths make the largest contribution to the signal. In addition, we can quantify the fit of the predicted geoid to the observed one by calculating the localized correlation and admittance between the two fields. While both the predicted and observed geoid are known up to degree and order 360 our analysis is limited to degrees between $L = 18$ and 180 (wavelengths of $\sim$2000–200 km). The maximum and minimum harmonic degree are constrained by the size of the elements in our model and the size of the model domain, respectively. The maximum element size is approximately $1°$ (near the model boundaries), corresponding to $L = 360$. The Nyquist frequency limits the analysis to half the maximum harmonic degree, $L = 180$. The model domain extends $45°$ in longitude and latitude, corresponding to $L = 9$. However, because the boundary conditions affect the slope of the topography at the model boundary, we choose a more conservative minimum harmonic degree corresponding to half the size of the box. This is equivalent to limiting our analysis at long wavelengths to signals with a least two wavelengths across the domain.

The localization method provides three quantities to assess the success of a given model: correlation, rms amplitude and admittance. A good fit to the observed geoid would have high (>0.8–0.9) positive correlations, non-zero rms amplitude and an admittance close to one over a large range of continuous positions and wavelengths. A high or low correlation where there is little power in the observed or predicted field is not considered significant. The correlation is sensitive to the position and structure of the fields, but not the amplitude. Admittance provides a measure of the ability of the dynamic model to predict the amplitude of the observed field: an admittance greater than or less than 1.0 indicates that the signal in the predicted field is too large or too small. Localized analyses of the predicted geoid for models 1, 3, 7 and 8 are presented in Figs 15–18 for cross-sections through the 3-D models at $28°S$ (results do not vary significantly along the trench).

The influence of the dynamic topography on the geoid is reinforced in the position and wavelength correlations for model 1 (Fig. 15). The offset of the geoid low towards the basin is seen in the high negative correlation from $180°$ to $185°$ at short wavelengths (high harmonic degree, $L = 100$–180). While there are small local regions of high correlations, these are also regions of low amplitude and admittance, and therefore are not considered significant. At longer wavelengths (1000–2000 km, $L = 36$–18), the difference in the slope of the geoid at the trench is seen in the large negative correlation from $175°$ to $200°$.

The best fit to the geoid is found for model 3 (Fig. 16), with a low-viscosity zone but no crustal density anomalies or low-density region within the wedge. The localization results include large positive correlations (>0.8) with the observed geoid at wavelengths of 250–1000 km ($L = 160$–36) over a 2000 km wide region across the trench. The rms amplitude is high throughout the region, while the admittance is slightly greater than 1.0, indicating that while the pattern of the geoid is well matched, the amplitude is too high. At the shortest wavelengths (<250 km), the correlation decreases rapidly and the admittance increases beneath the geoid low over the trench. The trench and the narrow basin remaining on the overriding plate
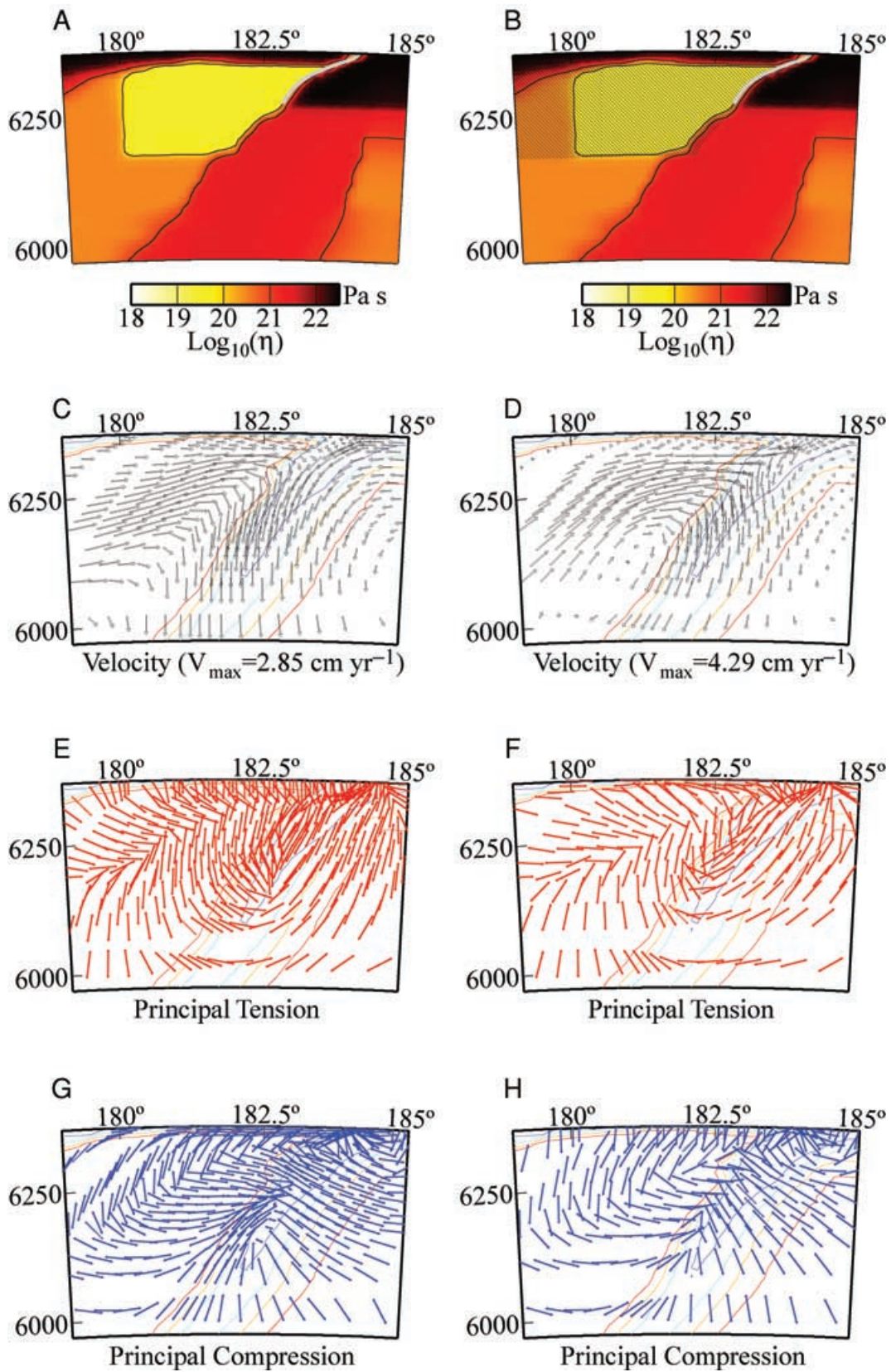
Figure 13. Comparison of stress orientation and flow for models 3 and 8. (a) Viscosity, (c) velocity field, (e) principal tension axes (red), and (g) principal compression axes (blue) for model 3. (b) Viscosity with location of wedge density anomaly indicated by hatched shading, (d) velocity field, (f) principal tension axes (red) and (h) principal compression axes (blue) for model 8. The thermal model is shown with colour contours (400 °C) in C–H for reference. Topography and geoid for these two models are show in Figs 11 and 12. Model 8, with a lower-density slab, low-viscosity and low-density wedge, has a stronger upward component of flow in the wedge (d) and extension in the overriding plate (f), while in model 3 the overriding plate is in compression (g).

A.

B.
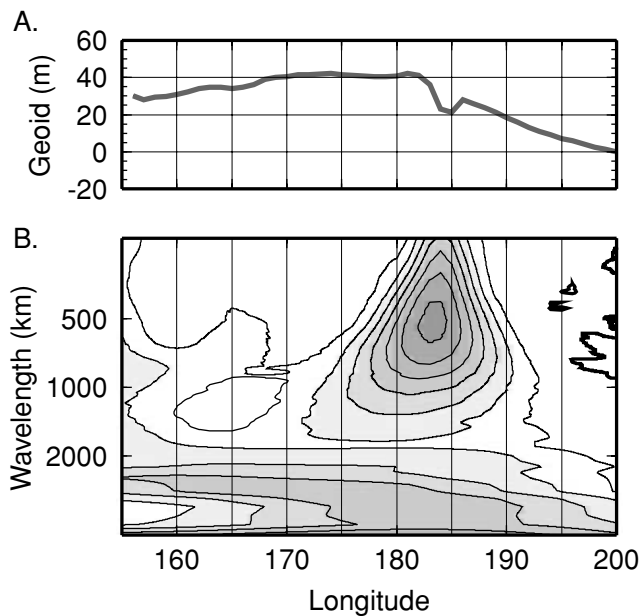
Figure 14. Localized rms amplitude for the observed geoid at 28°S. (a) Profile of the observed geoid with an east–west linear ramp is removed. (b) Position and wavelength (harmonic degree) dependent rms amplitude of the observed geoid. The contour interval is 0.5. Note that the localization analysis is fully 2-D and that the profiles are shown for reference.

cause the geoid low to broaden and widen, contributing to the misfit at the shortest wavelengths.

In order to match the observed topography, it was necessary to include sources of buoyancy in the crust and wedge. These sources of buoyancy increase the amplitude of positive topography at both short wavelengths over crustal buoyancy sources and long wavelengths over wedge buoyancy sources. The predicted geoid for models 4–7 and 9–10 are similar, with large amplitudes over the subduction zone (Fig. 12d–g). The correlation for model 7 (Fig. 17) has local regions of high positive correlation directly beneath the trench and to the east (at the shortest wavelengths), and further west, beneath the South Fiji Basin and Lord Howe Rise. Including the density anomaly from the thick crust of the Lord Howe Rise improves the correlation with the geoid at wavelengths of 400–1000 km over this feature. However, the admittance for the Lord Howe Rise is high (>2.5), while the admittance for the high correlation regions close to the subduction zone are greater than 2.0, indicating that these features have much larger amplitudes than are observed. This is clear over the trench, where the predicted signal has a peak-to-peak amplitude of 70 m, while the observed amplitude is only 40 m. The local regions of negative correlation at wavelengths of 700–1000 km east of the trench indicate that not only is the amplitude too large locally, the change in slope of the geoid approaching the subduction zone is also significantly different from that observed.

The large difference between the predicted geoid in models 3 and 7 is caused by the change in dynamic topography at the surface. Density anomalies very close to the surface are isostatically compensated by dynamic topography; that is, the contribution to the geoid from dynamic topography owing to the density anomaly is of the same magnitude and of opposite sign to the contribution arising from the density anomaly itself, so these contributions cancel out and there is no net contribution to the geoid. However, as the density anomaly is moved further from the surface, its contribution to the geoid decreases, while the contribution arising from dynamic
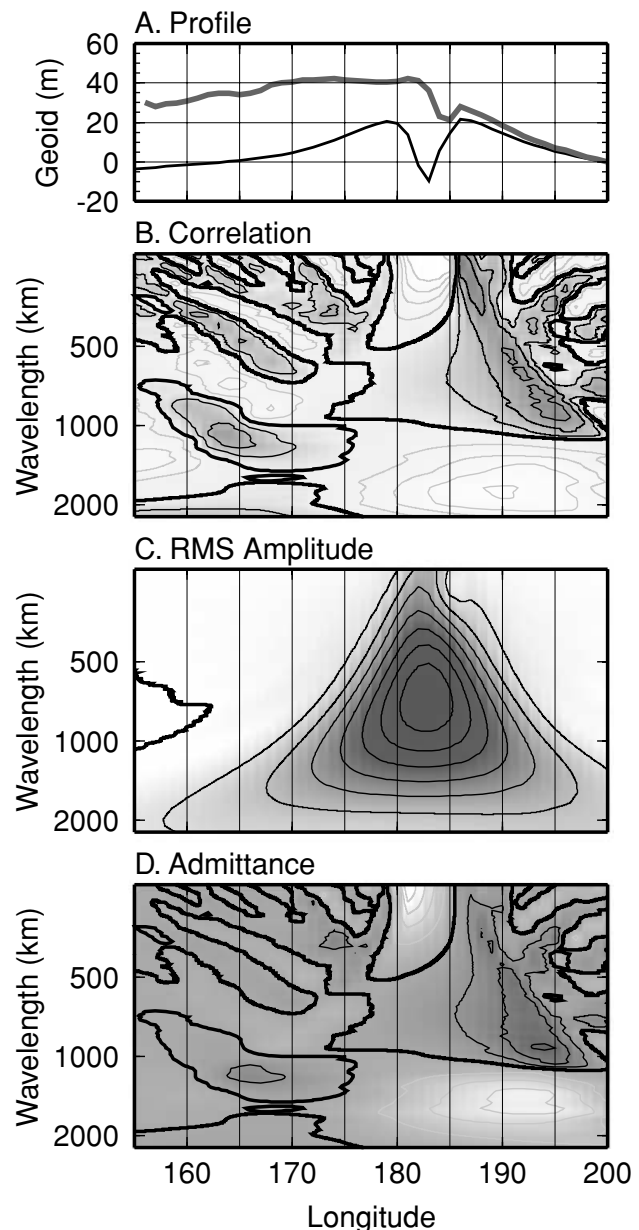
Figure 15. Geoid localization for model 1. (a) Cross-section of the observed (thick line) and the predicted (thin line) geoid at 28°S. An east–west linear ramp is removed from both profiles for comparison. (b) Position- and wavelength- (harmonic degree) dependent correlation between the observed and the predicted geoid. Positive values are indicated by dark regions and black contours. Negative values are indicated by light regions and grey contours. The zero contour is marked by the thick black contour. The contour interval is 0.2. (c) The rms amplitude of the model geoid. The contour interval is 1. (d) Admittance. Positive values are indicated by dark regions and black contours. Negative values are indicated by light regions and grey contours. The zero contour is marked by the thick black contour. The contour interval is 0.5.

topography depends on the viscosity structure. If the flow-induced density anomaly is of the same magnitude as the density anomaly within the mantle, its contribution to the geoid will be greater because it is closer to the surface. In models 5–11, the low-density region within the wedge is not near the surface and therefore causes dynamic topography that is not exactly compensated for by this deeper low-density anomaly. This leads to an overall increase in
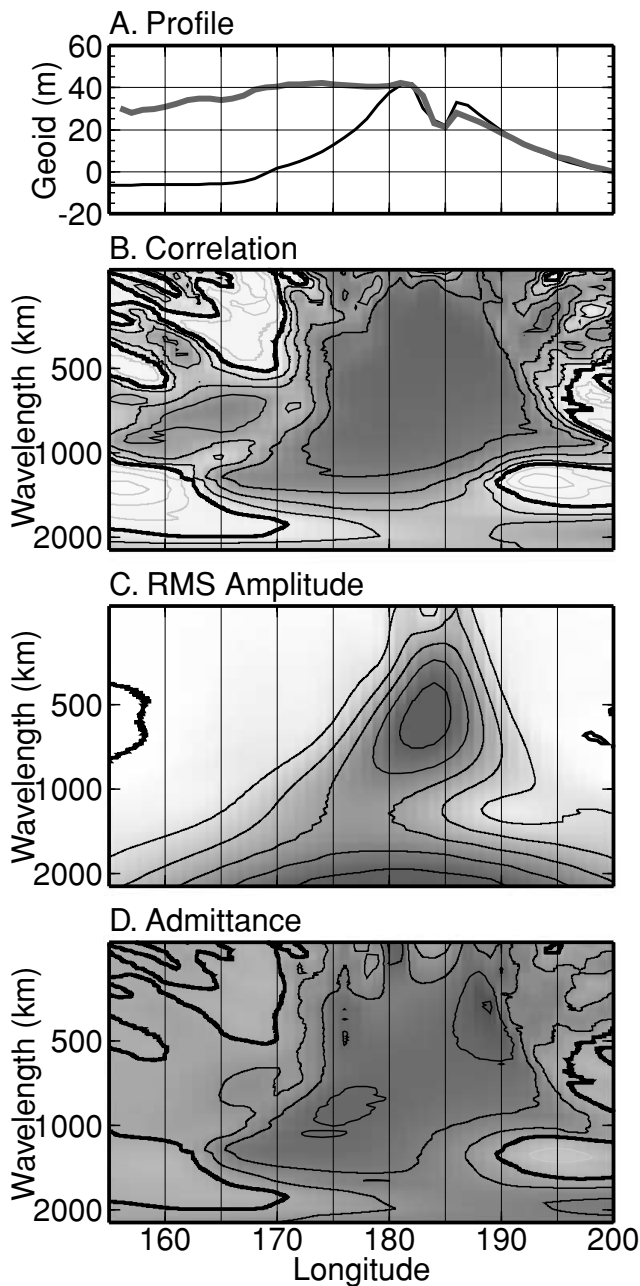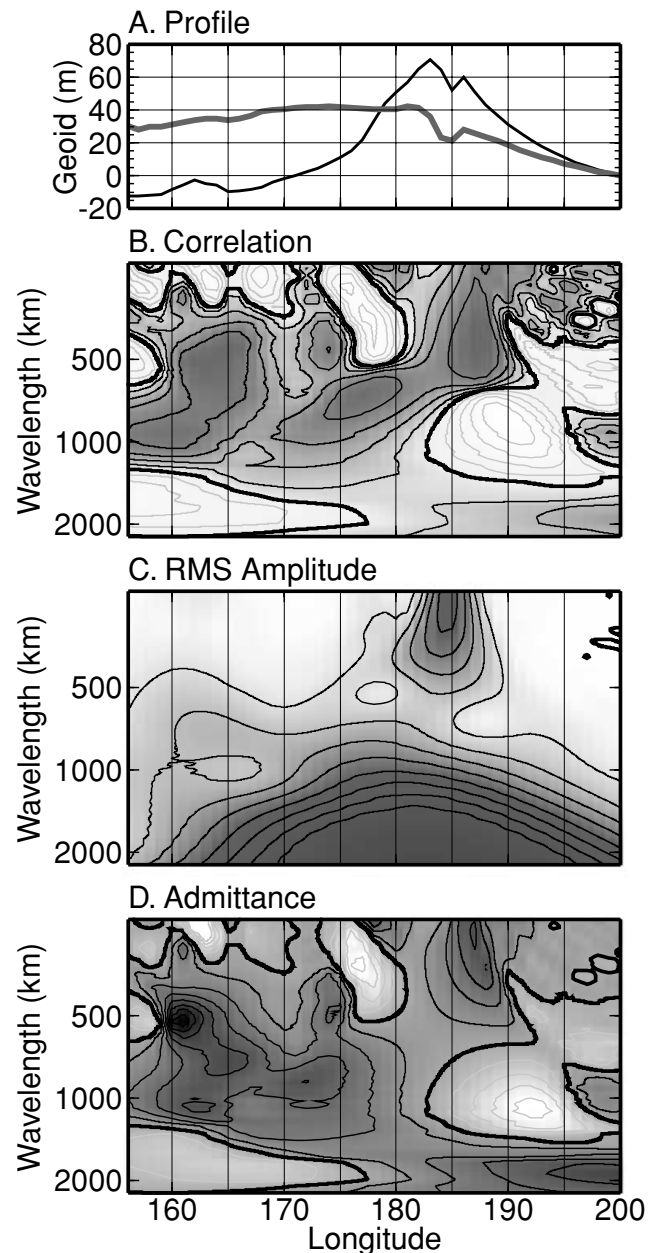
Figure 16. Geoid localization plots for Tonga model 3. The explanation is the same as in Fig. 15.

Figure 17. Geoid localization plots for Tonga model 7. The explanation is the same as in Fig. 15.

the amplitude of the geoid. Stated differently, in models 1–3 the large depression on the overriding plate, caused by the flow from the slab, partially compensates the positive geoid signal owing to the slab density, and this compensation decreases the geoid at short and long wavelengths.

The large amplitude of the geoid in model 7 indicates that either the positive dynamic topography predicted in these models is too high or the density of the slab is too large; these are the two positive contributions to the geoid. Since the predicted topography agrees well with the observed topography, this could be true if the low-density region we have included in the wedge extends too deep. Alternatively, we could match the observed topography with a shallower low-density region with a larger-density anomaly. The dynamic topography would then be more completely compensated

by the low-density region because it is closer to the surface, leading to less uncompensated positive dynamic topography. However, this change would have the largest effect over the backarc region, west of the trench, and would have less of an effect directly beneath the trench where the slab is closest to the surface and therefore has the largest effect on the geoid. Decreasing the density of the slab will also affect dynamic topography, but as can be seen in Fig. 10, because the low-viscosity region decouples the slab from the overriding plate, the main effect on topography is to decrease the trench depth and topography on the overriding plate within 50 km of the fault (in the forearc).

The correlation with the observed geoid does improve when the slab density is decreased by a factor of 1.3 (model 8, Fig. 18) keeping other density anomalies the same as in model 7. The correlation over a 1000 km wide region beneath the subducting plate, trench and
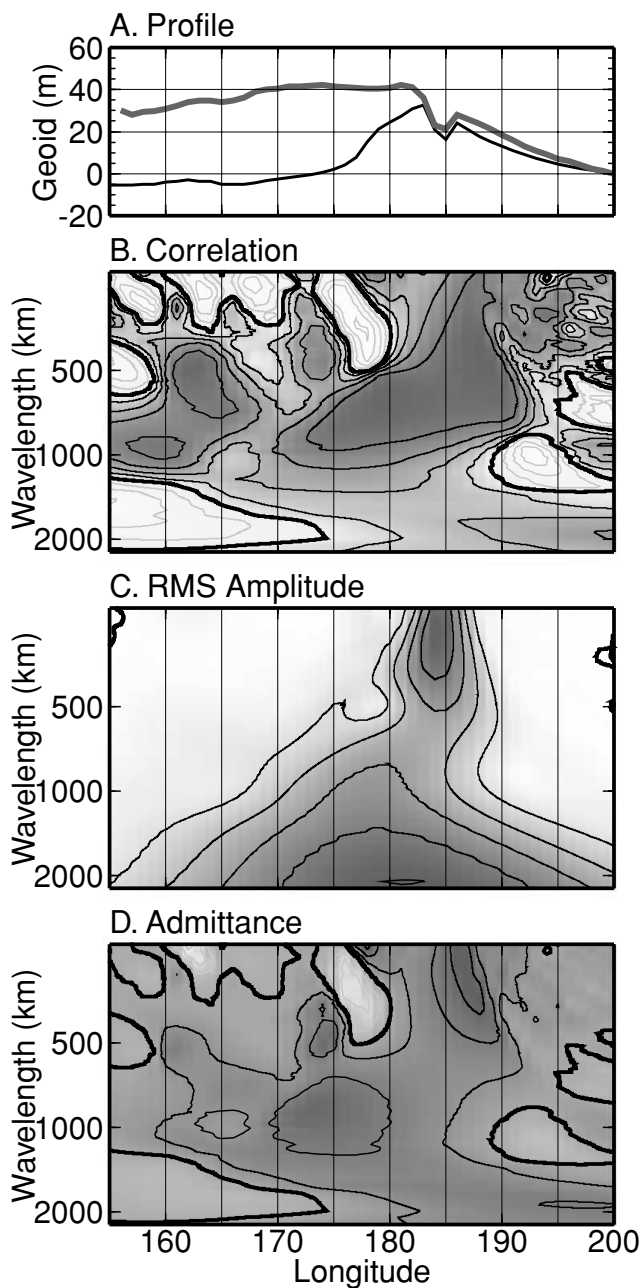
Figure 18. Geoid localization plots for Tonga model 8. The explanation is the same as in Fig. 15.

backarc region is greater than 0.8 at wavelengths ranging from 200 to 1000 km. The rms amplitude is high throughout these regions and the admittance is 0.75–1.5, with the highest values occurring at the shortest wavelengths beneath the trench. In addition, the thickness of the continental crustal anomalies are reduced in this model from 20 to 28 km in order to better match the observed topography over these regions. With this change the correlation across the Lord Howe Rise remains high, while the admittance is reduced to 0.8.

In models 1–10, it is assumed that the density anomaly caused by basaltic crust in the subducting plate contributes little to the geoid owing to the small volume of unconverted basalt and harzburgite above the basalt-to-eclogite transition. In model 11, we test whether a delayed basalt-to-eclogite transition can explain the difference between the predicted geoid in model 7 and the observed geoid. We

find that including the density anomaly for the basalt and harzburgite layers down to 150 km does decrease the peak height of the geoid over the subduction zone by 10 m. However, it also deepens the short-wavelength geoid low directly over the trench, degrading the fit to the geoid at short wavelengths. From this model, we conclude that such a deep basalt-to-eclogite transition is not present in the Tonga–Kermadec slab, and the density anomaly from unconverted basalt cannot explain the discrepancy between the model and the observed geoid.

Although the agreement between the predicted and observed geoid is better in model 3 than in model 8, the constraint we have imposed to match both the topography and the geoid simultaneously leads us to conclude that model 8 is, in fact, a better model of the dynamics in the region of the Tonga–Kermadec Trench. In addition, model 8 has an extension in the overriding plate, providing a better match to the observed stress orientation. The lack of agreement west of the backarc is, in fact, expected because there are other known sources of positive density anomalies (e.g. the New Hebrides slab) that are not included in this model. Other deeper positive anomalies may also be important as illustrated by the increase in the intermediate- to long-wavelength geoid (500–2000 km) in models 9 and 10. Tomography models of the Tonga–Kermadec region have a high-velocity region extending west of the slab along the 670 km discontinuity (van der Hilst 1995; Zhao *et al.* 1997). There is some debate as to whether this seismic anomaly reflects a slab that is attached to the Tonga–Kermadec slab or is the remnant of Pacific Plate subduction southward along the Vitiaz Trench (Brudzinski & Chen 2000; Chen & Brudzinski 2001).

7 DISCUSSION AND CONCLUSIONS

This study set out to investigate the influence of lateral variations in viscosity on several observations, which could then be used to constrain the 3-D viscosity and buoyancy structure within the Tonga–Kermadec subduction zone and to provide a self-consistent model of the dynamics over a broad range of length-scales. We have explored the influence of radial viscosity structure, slab viscosity, a low-viscosity wedge and variable age lithosphere on the flow, stress field, dynamic topography and geoid. We find that by including density anomalies as a result of lithosphere age, crustal thickness and chemical changes within the wedge, we can model both the long- and short-wavelength topography. A fault included along the plate boundary is needed to form the trench and develop asymmetric subduction. However, numerical limitations prevent us from accurately modelling the depth of the trench or constraining the lateral viscosity structure within the trench or plate coupling along the fault. By limiting the trench depth to the observed depth (5 km) in calculating the geoid, we feel confident that the geoid results are robust at all but the very shortest wavelengths (less than 50 km) directly over the trench. Therefore, the conclusion that the slab density, based on the thermal anomaly for the Tonga–Kermadec slab, is too large is not likely to change when these numerical limitations are overcome.

Several aspects of the preferred viscosity structure derived from the 2-D models are consistent with previous modelling results (see Section 1): a moderate increase in viscosity from the upper to the lower mantle is necessary to match observations of down-dip stress orientation within the slab and to limit the height of the forebulge on the subducting plate to values consistent with observations (∼500 m). We have also shown how different aspects of the viscosity structure affect different observations and have placed stronger constraints on the range of viscosity values permitted. The

magnitude of the observed strain rate provides a strong constraint on the absolute viscosity of the Tonga–Kermadec slab, requiring that the viscosity be less than 3×10^{23} Pa s. The orientation of stress and coupling of flow between the slab and lithosphere require that the slab is weaker than the lower mantle, but not more than a factor of 100 weaker than the lithosphere within the subduction zone.

While several observations are easily explained by accounting for the strength of the slab and an increase in viscosity from the upper to lower mantle, other observations require a low-viscosity region in the wedge, a low-density region in the wedge and/or a reduction in the inferred density of the slab. In particular, we have found that several observations, not previously reproduced in a dynamic model, are a natural consequence of including a low-viscosity wedge (independent of temperature) within a radial- and temperature-dependent viscosity structure. These results include down-dip compression within the shallow portion of the slab, extension of the overriding plate and positive dynamic topography on the overriding plate.

The change in stress orientation within the shallow portion of the slab, from down-dip tension to down-dip or near down-dip compression when the wedge viscosity is decreased, reflects a change in the mode of deformation within the slab. Two distinct modes of slab deformation characterized by differences in the flow and orientation of stress are observed. If the ratio of slab to wedge (or asthenosphere) viscosity is small, then the slab is strongly coupled to the larger-scale flow within the subduction zone. The orientation of stress within the slab indicates that the slab flows into the mantle as a dense viscous body falling under its own weight. However, if the slab viscosity is increased or a low-viscosity wedge is included, then the orientation of stress and pattern of flow are consistent with viscous flexure: the slab bends more than flows in response to the load of the deeper portion of the slab, independent of the surrounding flow.

Horizontal extension and a decrease in the basin size on the overriding plate are a consequence of decoupling the downward flow of the slab from the surface. Compression of the overriding plate observed in models without an LVW is caused by the downward flow of the slab directly beneath the basin, and not by the horizontal flow of the lithosphere at the trench, since this component of convergence is focused along the boundary fault. The change in the stress orientation on the overriding plate to extension when a low-viscosity region is included in the models, indicates that the presence of backarc spreading regions may be a local dynamic response rather than simply a result of global plate motions.

In addition to providing a self-consistent explanation of geophysical observations within the Tonga–Kermadec subduction zone, a low-viscosity region in the wedge is consistent with geochemical, petrologic and rock mechanics observations of other processes occurring within the wedge. In order to match the observed topography, it was necessary to include variations in lithosphere age, crustal thickness and a broad region of low-density ($\Delta \rho = 20$ kg m^{-3}) material in the wedge. If the LVW is caused by water within the wedge from dehydration of the slab, as we have proposed, then a lower-density region within the wedge is consistent with the higher degrees of melting and depletion of the wedge material expected in the presence of high concentrations of water. The fact that both of these changes are needed to match the geophysical observations strengthens our conclusion that the LVW is a self-consistent feature of the viscosity structure and an integral part of subduction zone dynamics.

We find that, in the 2-D models with young lithosphere above the wedge, the width of the low-viscosity region is not constrained. The need for a low-density region several hundreds of kilometres from the slab indicates that the low-viscosity region may also extend far from the slab. This result has important implications for the transport of fluids in the wedge and large-scale flow above the slab. As shown for the 2-D model with a large low-viscosity and low-density region, a reversal of flow occurs at the edge of the low-viscosity region. In the 3-D models, this edge corresponds to the location of backarc spreading above the slab. It is not possible to know from our instantaneous models of flow whether this is coincidence, or whether a buoyant, low-viscosity region is the result of or the cause of backarc spreading. Previous attempts to explain backarc spreading have included: differences in the absolute plate motion of the overriding and subducting plate (Chase 1978), and the influence of trench roll-back on the stress of the overriding plate (Scholz & Campos 1995; Seno & Yamanaka 1998). While both of these mechanisms may take part in determining whether the overriding plate is in extension, the LVW provides an additional, local mechanism, for backarc spreading consistent with explanations of slab roll-back being caused by less coupling to the overriding plate, and the observation that subduction zones with slabs in down-dip compression also have backarc spreading (Seno & Yamanaka 1998).

The shallow bathymetry of the overriding plate in the Tonga–Kermadec subduction zone persists far from the active region of backarc spreading into the region of previous episodes of island-arc and backarc magmatism. By extending the region of low-density material further from the slab (an additional 500 km) we are able to match the observed shallow bathymetry. This suggests that as the trench shifts locations or retreats as a result of slab roll-back, the regions of low-density material created within the wedge may be left behind.

The effect of the low-viscosity and low-density region on dynamic topography has important implications for previous ideas concerning the compensation of density anomalies within the Earth by density anomalies owing to flow-induced dynamic topography. Hager (1984) found that both a jump in viscosity and an increase in the density associated with slabs (by extending them beyond 670 km depth) was necessary to match the long-wavelength geoid. Both of these conclusions were necessary to overcome the large negative contribution to the geoid from the dynamic topography above slabs. We find that lateral variations in viscosity modify the flow owing to the slab and significantly decrease the amount of negative dynamic topography and the length-scales over which topography exists. If we also include shallow, low-density anomalies in an effort to match the short- to intermediate-wavelength topography, then we find that the shallow density of the slab is too large, a very different result from that found for the long-wavelength geoid.

It is possible to match the shallow topography on the overriding plate with shallower-density anomalies, which would then contribute less to uncompensated dynamic topography, by contributing less to flow within the wedge. However, by decreasing the depth extent over which these density anomalies occur, the amplitude of the density anomalies would need to increase proportionally. The density anomaly needed to match the observed topography within a region extending to a depth of 200 km is -20 kg m^{-3}. Below 100 km depth this anomaly is attributed to reduction in the amount of garnet in highly depleted peridotite. Above 100 km, the anomaly is equivalent to having 4 wt per cent *in situ* melt with a density of 2700 kg m^{-3}, a rather high *in situ* melt concentration to begin with. Therefore, limiting the depth over which this low-density material exists to the shallowest parts of the mantle would require unreasonable melt concentrations. In addition, since this low-density region may be needed to match the shallow bathymetry far west of the spreading centre, it appears unlikely that high concentrations of melt within the crust could explain the shallow topography. Therefore, in our

models the only way to match both the shallow topography on the overriding plate and the geoid is to decrease the density of the slab.

While our models do not constrain the exact depth range over which slab density must decrease, the localization results indicate that the upper-mantle portion of the slab (100–400 km) directly beneath the trench and island arc needs to be less dense than predicted based on the thermal model used. However, there are several physical or geochemical processes that are not included in our models, which could decrease the density of the slab.

(1) The thermal anomaly of the slab in our models, based on flow in a uniform viscosity asthenosphere, may be an overestimate. The change in flow caused by a low-viscosity wedge would probably lead to steeper temperature gradients along the top surface of the slab, causing the slab to heat up more quickly. This would lead to a cooler mantle, but would distribute the density anomaly over a larger length-scale. However, it is difficult to estimate what effect the LVW will have on the thermal anomaly of the slab without performing the fully dynamic, time-dependent calculation.

(2) Our models also neglect shear heating along the plate boundary fault. Based on analytical estimates of pressure–temperature–time paths, shear heating on the plate boundary fault at shallow depths (15–50 km) could increase the temperature of the slab surface by 200–300 °C, (with a convergence rate of 10 cm yr^{-1} and a shear stress of 40 MPa), if shear coupling occurs over a narrow zone (2 km) (Peacock 1992). This could lead to a decrease in slab density of 10 kg m^{-3}, owing to the initial temperature change, and could lead to an additional decrease in density by increasing the temperature gradient at the slab surface, allowing the slab at deeper depths to heat up more quickly. However, this estimate is an upper bound, as it assumes a very narrow fault zone and a relatively large shear stress.

(3) If metastable olivine exists within the core of the slab owing to a delayed phase transition at 410 km, this would lead to a low-density region ($\Delta\rho = 273$ kg m^{-3}) within the slab below 410 km. The volume of metastable olivine involved depends strongly on the temperature within the slab and the kinetics of the transformation (Mosenfelder *et al.* 2001). However, this reduction in the relative density of the slab occurs deeper than the low-density region required by the numerical models, and therefore would probably contribute to the longer-wavelength geoid.

(4) Partial support of the weight of the slab by elastic stresses is unlikely since previous models with visco-elastic rheology produce a similar topography to models with only viscous rheology (Gurnis *et al.* 1996).

(5) Basaltic crust in the subducting plate may decrease the net density anomaly of the subducting slab at shallow depths. Model 11, which includes the density anomaly owing to the unconverted basaltic crust extending to 150 km depth, demonstrates that while this density anomaly does decrease the geoid anomaly at intermediate wavelengths by 10 m, the volume of basaltic crust is too small to account for the discrepancy in the geoid at these wavelengths and degrades the fit to the geoid at shorter wavelengths.

Several of the results discussed have important implications for time-dependent processes within the subduction zone: backarc spreading, trench roll-back and the thermal anomaly of the slab, which cannot be fully addressed by instantaneous dynamic models. However, in using several different observations, the instantaneous models allow us to fully investigate the sensitivity of these observations to different aspects of the viscosity and buoyancy structure over a wide range of length-scales. In doing so we have found that subduction zone dynamics are strongly dependent on lateral vari-

ations in viscosity and that short-wavelength structure can affect both the short- and long-wavelength dynamics. Finally, using several observations and a multiscale analysis of the geoid, we have found that the Tonga–Kermadec subduction zone probably has a low-viscosity and a low-density region in the wedge and that the density of the slab may be smaller than predicted by simple thermal models. In the future, a similar multiscale approach applied to time-dependent models including a low-viscosity wedge will be needed to explore the evolution of the wedge and slab thermal structure in a self-consistent dynamic model.

REFERENCES

Apperson, K.D. & Frohlich, C., 1987. The relationship between Wadati–Benioff Zone geometry and *P*, *T* and *B* axes of intermediate and deep focus earthquakes, *J. geophys. Res.,* **92,** 13 821–13 831.

Barazangi, M. & Isacks, B., 1971. Lateral variations of seismic-wave attenuation in the upper mantle above the inclined earthquake zone of the Tonga Island Arc: deep anomaly in the upper mantle, *J. geophys. Res.,* **76,** 8493–8515.

Batchelor, G.K., 1967. *An Introduction to Fluid Dynamics,* Cambridge University Press, Cambridge.

Bevis, M., 1988. Seismic slip and down-dip strain rates in Wadati–Benioff Zones, *Science,* **240,** 1317–1319.

Billen, M.I. & Gurnis, M., 2001. A low-viscosity wedge in subduction zones, *Earth planet. Sci. Lett.,* **193,** 227–236.

Billen, M.I. & Stock, J., 2000. Origin and morphology of the Osbourn Trough, *J. geophys. Res.,* **105,** 13 481–13 489.

Bodine, J.H. & Watts, A.B., 1979. On lithospheric flexure seaward of the Bonin and Mariana Trenches, *Earth Planet. Sci. Lett.,* **43,** 132–148.

Bostock, M.G., Hyndman, R.D., Roodenay, S. & Peacock, S.M., 2002. An inverted continental Moho and serpentinization of the forearc mantle, *Nature,* **417,** 536–538.

Brudzinski, M.R. & Chen, W.-P., 2000. Variations in P wave speeds and outboard earthquakes: evidence for a petrologic anomaly in the mantle transition zone, *J. geophys. Res.,* **105,** 21 661–21 682.

Buiter, S.J.H., Govers, R. & Wortel, M.J.R., 2001. A modelling study of vertical surface displacements at convergent plate margins, *Geophys. J. Int.,* **147,** 415–427.

Chase, C.G., 1978. Extension behind island arcs and motions relative to hot spots, *J. geophys. Res.,* **83,** 5385–5387.

Chen, W.-P. & Brudzinski, M.R., 2001. Evidence for a large-scale remnant of subducted lithosphere beneath Fiji, *Science,* **292,** 2475–2479.

Conrad, C.P. & Hager, B.H., 1999. Effects of plate bending and fault strength at subduction zones on plate dynamics, *J. geophys. Res.,* **104,** 17 551–17 571.

Davies, J.H. & Stevenson, D.J., 1992. Physical model of the source region of subduction zone volcanics, *J. geophys. Res.,* **97,** 2037–2070.

DeBremaecker, J.C., 1977. Is the oceanic lithosphere elastic or viscous?, *J. geophys. Res.,* **82,** 2001–2004.

GEBCO, 1997. General Bathymetric Chart of the Oceans, British Oceanographic Data Centre, Computer file.

Gurnis, M., Eloy, C. & Zhong, S., 1996. Free-surface formulation of mantle convection—II. Implication for subduction-zone observables, *Geophys. J. Int.,* **127,** 719–727.

Hager, B.H., 1984. Subducted slabs and the geoid: constraints on mantle rheology and flow, *J. geophys. Res.,* **89,** 6003–6015.

Hager, B.H. & Clayton, R.W., 1989. Constraints on the structure of mantle convection using seismic observations, flow models, and the geoid, in *Mantle Convection,* Chap. 9, pp. 657–764, Gordon and Breach, New York.

Hager, B.H. & O'Connell, R.J., 1981. A simple global model of plate dynamics and mantle convection, *J. geophys. Res.,* **86,** 4843–4867.

Hager, B.H. & Richards, M.A., 1989. Long-wavelength variations in Earth's geoid: physical models and dynamical implications, *Phil. Trans. R. Soc. Lond.,* A., **328,** 309–327.

Hager, B.H., Clayton, R.W., Richrads, M.A., Comer, R.P. & Dziewonski, A.M., 1985. Lower mantle heterogeneity, dynamic topography and the geoid, *Nature,* **313,** 541–545.

Hasegawa, A., Zhao, D., Hori, S., Yamamoto, A. & Horiuchi, S., 1991. Deep structure of the Northeastern Japan Arc and its relationship to seismic and volcanic activity, *Nature,* **352,** 683–689.

Hirth, G. & Kohlstedt, D.L., 1996. Water in the oceanic upper mantle: implications for rheology, melt extraction and the evolution of the lithosphere, *Earth planet. Sci. Lett.,* **144,** 93–108.

Holt, W.E., 1995. Flow fields within the Tonga slab determined from the moment tensors of deep earthquakes, *Geophys. Res. Lett.,* **22,** 989–992.

Houseman, G.A. & Gubbins, D., 1997. Deformation of subducted oceanic lithosphere, *Geophys. J. Int.,* **131,** 535–551.

Hughes, T.J.R., 1987. *The Finite Element Method,* Prentice-Hall, Englewood Cliffs, NJ.

Isacks, B. & Molnar, P., 1971. Distribution of stress in descending lithosphere from a global survey of focal-mechanism solutions of mantle earthquakes, *Rev. Geophys. Space Phys.,* **9,** 103.

Jacoby, M.J. & Schmeling, H., 1982. On the effects of the lithosphere on mantle convection and evolution, *Phys. Earth planet. Inter.,* **29,** 305–319.

Karato, S., 2003. Mapping water content in the upper mantle, in *Subduction Factory, AGU Monograph,* ed. Eiler, J., American Geophysical Union, Washington, DC, in press.

Karato, S. & Jung, H., 1998. Water, partial melting and the origin of the seismic low velocity and high attenuation zone in the upper mantle, *Earth planet. Sci. Lett.,* **157,** 193–207.

Karato, S. & Jung, H., 2003. Effects of pressure on high-temperature dislocation creep in olivine, *Philos. Magazine Ann.,* in press.

Karato, S.-I. & Karki, B.B., 2001. Origin of lateral variation of seismic wave velocities and density in the deep mantle, *J. geophys. Res.,* **106,** 21 771–21 783.

Kelemen, P.B., Hirth, G., Shimizu, N., Spiegelman, M. & Dick, H.J.B., 1997. A review of melt migration processes in the adiabatically upwelling mantle beneath spreading ridges, *Phil. Trans. R. Soc. Lond.,* A, **355,** 283–318.

King, S.D., 1995. Models of mantle viscosity, in, *Mineral Physics and Crystallography, AGU Reference Shelf,* pp. 227–236, American Geophysical Union.

Koch, D.M. & Ribe, N.M., 1989. The effect of lateral viscosity variations on surface observables, *Geophys. Res. Lett.,* **16,** 535–538.

Kohlstedt, D.L., Evans, B. & Mackwell, S.J., 1995. Strength of the lithosphere: constraints imposed by laboratory experiments, *J. geophys. Res.,* **100,** 17 587–17 602.

Kohlstedt, D.L., Keppler, H. & Rubie, D.C., 1996. Solubility of water in a, b, and g phases of $(Mg,Fe)_2SiO_4,,$ *Contrib. Mineral. Petrol.,* **123,** 345–357.

Kostrov, V.V., 1974. Seismic moment and energy of earthquakes, and seismic flow of rock, *Earth Phys.,* **1,** 13–20.

Kroenke, L.W., 1984. *Cenozoic Tectonic Development of the Southwest Pacific,* UN ESCAP CCOP/SOPAC Tech. Bull. 6, New Zealand.

Lambeck, K., 1988. *Geophysical Geodesy: the Slow Deformations of the Earth,* Oxford University Press, Oxford.

Lee, M. & Powell, R., (eds) 1982. *Initial Reports of the Deep Sea Drilling Program,* Chap. 1, pp. 4–45, US Government Printing Office, Washington, DC.

Lemoine, F.G. *et al.*, 1998. The development of the Joint NASA GSFC and NIMA Geopotential Model EGM96, Tech. rep., NASA Goddard Space Flight Center, Greenbelt, Maryland.

McAdoo, D.C., 1982. On the compensation of geoid anomalies due to subducting slabs, *J. geophys. Res.,* **87,** 8684–8692.

McKenzie, D.P., 1969. Speculations on the consequences and causes of plate motions, *Geophys. J. R. astr. Soc.,* **18,** 1–32.

Mei, S., 1999. The effect of water on the plastic deformation of olivine and olivine-basalt aggregates, *PhD thesis,* University of Minnesota.

Melosh, H.J., 1978. Dynamic support of the outer rise, *Geophys. Res. Lett.,* **5,** 321–324.

Moresi, L. & Gurnis, M., 1996. Constraints on the lateral strength of slabs from three-dimensional dynamic flow models, *Earth planet. Sci. Lett.,* **138,** 15–28.

Moresi, L.N. & Solomatov, V.S., 1995. Numerical investigations of two-dimensional convection with extremely large viscosity variations, *Phys. Fluid.,* **9,** 2142–2162.

Moresi, L., Zhong, S. & Gurnis, M., 1996. The accuracy of finite element solutions of Stokes' flow with strongly varying viscosity, *Earth planet. Sci. Lett.,* **97,** 83–94.

Morris, J.D., Leeman, W.P. & Tera, F., 1990. The subducted component in island-arc lavas: constraints from Be isotopes and B–Be systematics, *Nature,* **344,** 31–36.

Mosenfelder, J.L., Marton, F.C., II, C.R.R., Kerschhofer, L. & Rubie, D.C., 2001. Experimental constraints on the depth of olivine metastability in subducting lithosphere, *Phys. Earth planet. Inter.,* **127,** 165–180.

Müller, R.D., Royer, J.Y. & Lawver, L.A., 1993. Revised plate motions relative to the hot spots from combined Atlantic and Indian hotspot tracks, *Geology,* **21,** 275–278.

Nothard, S., Haines, J., Jackson, J. & Holt, B., 1996. Distributed deformation in the subducting lithosphere at Tonga, *Geophys. J. Int.,* **127,** 328–338.

Ogawa, Y., Kobayashi, K., Hotta, H. & Fujioka, K., 1997. Tension cracks on the oceanward slopes of the northern Japan and Mariana trenches, *Marine Geol.,* **141,** 111–123.

Peacock, S.M., 1992. Blueschist-facies metamorphism, shear heating, and P– T –t paths in subduction shear zones, *J. geophys. Res.,* **97,** 17 693–17 707.

Peacock, S.M. & Wang, K., 1999. Seismic consequences of warm versus cool subduction metamorphism: examples from Southwest and Northeast Japan, *Science,* **286,** 937–939.

Raitt, R.W., Fisher, R.L. & Mason, R.G., 1955. Tonga Trench, in, *Geological Society of America, Special Paper, Crust of the Earth,* Vol. 62, pp. 237–254, Waverly Press, Baltimore, MD.

Ravine, M.A. & Morgan, J.P., 1993. Geoid effects of lateral viscosity variations near the top of the mantle: a 2-D model, *Earth planet. Sci. Lett.,* **119,** 617–625.

Ricard, Y., Froidevaux, C. & Fleitout, L., 1988. Global plate motion and the geoid: a physical model, *Geophys. J.,* **93,** 477–484.

Richards, M.A. & Hager, B.H., 1984. Geoid anomalies in a dynamic Earth, *J. geophys. Res.,* **89,** 5987–6002.

Richards, M.A. & Hager, B.H., 1989. Effects of lateral viscosity variations on long-wavelength geoid anomalies an topography, *J. geophys. Res.,* **94,** 10 299–10 313.

Ringwood, A.E., 1982. Phase transformations and differentiation in subducted lithosphere: implications for mantle dynamics, basalt petrogenesis, and crustal evolution, *J. Geol.,* **90,** 611–643.

Roth, E.G., Wiens, D.A., Dorman, L.M., Hildebrand, J. & Webb, S.C., 1999. Seismic attenuation tomography of the Tonga–Fiji region using phase pair methods, *J. geophys. Res.,* **104,** 4795–4809.

Roth, E., Wiens, D. & Zhao, D., 2000. An empirical relationship between seismic attenuation and velocity anomalies in the upper mantle, *Geophys. Res. Lett.,* **27,** 601–604.

Sabadini, R., Giunchi, C., Gasperini, P. & Boschi, E., 1992. Plate motion and dragging of the upper mantle: lateral variations of lithospheric thickness and their implications for intraplate deformation, *Geophys. Res. Lett.,* **19,** 749–752.

Scholz, C.H. & Campos, J., 1995. On the mechanism of seismic coupling and back-arc spreading at subduction zones, *J. geophys. Res.,* **100,** 22 103–22 115.

Seno, T. & Yamanaka, Y., 1998. Arc stresses determined by slabs: implications for mechanisms of back-arc spreading, *Geophys. Res. Lett.,* **25,** 3227–3230.

Simons, M., 1996. Localization of gravity ond topography: constraints on the tectonics and mantle dynamics of Earth and Venus, *PhD thesis,* Massachusetts Insititute of Technology, Boston, MA.

Simons, M., Solomon, S. & Hager, B.H., 1997. Localization of gravity and topography: constraints on the tectonics and mantle dynamics of Venus, *Geophys. J. Int.,* **131,** 24–44.

Sleep, N.H., 1975. Stress and flow beneath island arcs, *Geophys. J. Int.,* **42,** 827–857.

Stein, S. & Stein, C., 1996. Thermo-mechanical evolution of oceanic lithosphere: implications for the subduction process and deep earthquakes, in *Subduction Top to Bottom,* **96,** pp. 1–17, Geophysical Monograph, American Geophysical Union.

Stolper, E. & Newman, S., 1994. The role of water in the petrogenesis of Mariana trough magmas, *Earth planet. Sci. Lett.,* **121,** 293–325.

Tatsumi, Y., Sakayuma, M., Fukuyama, H. & Kushiro, I., 1983. Generation of arc basalt magmas and thermal structure of the mantle wedge in subduction zones, *J. geophys. Res.,* **88,** 5815–5825.

Thoraval, C. & Richards, M.A., 1997. The geoid constraint in global geodynamics: viscosity structure, mantle heterogeneity models and boundary conditions, *Geophys. J. Int.,* **131,** 1–8.

Torrance, K.E. & Turcotte, D.L., 1971. Thermal convection with large viscosity variations, *J. Fluid Mech.,* **47,** 113–125.

Turcotte, D.L., McAdoo, D.C. & Caldwell, J.G., 1978. An elastic–perfectly plastic analysis of the bending of the lithosphere at a trench, *Tectonophysics,* **47,** 193–208.

van der Hilst, R., 1995. Complex morphology of subducted lithosphere in the mantle beneath the Tonga Trench, *Nature,* **374,** 154–157.

Vassiliou, M.S., Hager, B.H. & Raefsky, A., 1984. The distribution of earthquakes with depth and stress in subducting slabs, *J. Geodyn.,* **1,** 11–28.

Vigny, C., Ricard, Y. & Froidevaux, C., 1991. The driving mechanism of plate tectonics, *Tectonophysics,* **187,** 345–360.

Wen, L. & Anderson, D.L., 1997. Present-day plate motion constraint on mantle rheology and convection, *J. geophys. Res.,* **102,** 24 639–24 653.

Wessel, P. & Smith, W.H.F., 1995. New version of the generic mapping tools released, *EOS, Trans. Am. geophys. Un.,* **76,** 329.

Zhang, S. & Christensen, U., 1993. Some effects of lateral viscosity variations on geoid and surface velocities induced by density anomalies in the mantle, *Geophys. J. Int.,* **114,** 531–546.

Zhao, D., Hasegawa, A. & Horiuchi, S., 1992. Tomographic imaging of *P* and *S* wave velocity structure beneath Northeastern Japan, *J. geophys. Res.,* **97,** 19 909–19 928.

Zhao, D., Xu, Y., Wiens, D.A., Dorman, L., Hildebrand, J. & Webb, S., 1997. Depth extent of the Lau back-arc spreading center and its relation to subduction processes, *Science,* **278,** 254–257.

Zhong, S., 1996. Analytic solutions for Stokes' flow with lateral variations in viscosity, *Geophys. J. Int.,* **124,** 18–28.

Zhong, S. & Davies, G.F., 1999. Effects of plate and slab viscosities on the geoid, *Earth planet. Sci. Lett.,* **170,** 487–496.

Zhong, S. & Gurnis, M., 1992. Viscous flow model of a subduction zone with a faulted lithosphere: long and short wavelength topography, gravity and geoid, *Geophys. Res. Lett.,* **19,** 1891–1894.

Zhong, S. & Gurnis, M., 1994. Controls on trench topography from dynamic models of subducted slabs, *J. geophys. Res.,* **99,** 15 683–15 695.

Zhong, S. & Gurnis, M., 1996. Interaction of weak faults and non-Newtonian rheology produces plate tectonics in a 3-D model of mantle flow, *Nature,* **383,** 245–247.

Zhong, S., Gurnis, M. & Hulbert, G., 1993. Accurate determination of surface normal stress in viscous flow from a consistent boundary flux method, *Phys. Earth planet. Inter.,* **78,** 1–8.

Zhong, S., Gurnis, M. & Moresi, L., 1996. Free-surface formulation of mantle convection—I. Basic theory and application to plumes, *Geophys. J. Int.,* **127,** 708–718.

Zhong, S., Gurnis, M. & Moresi, L., 1998. Role of faults, nonlinear rheology, and viscosity structure in generating plates from instantaneous mantle flow models, *J. geophys. Res.,* **103,** 15 255–15 268.

Zhong, S., Zuber, M.T., Moresi, L. & Gurnis, M., 2000. Role of temperature-dependent viscosity and surface plates in spherical shell models of mantle convection, *J. geophys. Res.,* **105,** 11 063–11 082.

APPENDIX A: TRANSFORMATION OF CITCOM WITH FAULTS TO SPHERICAL GEOMETRY

We developed CitcomT to solve viscous flow problems with faults in a spherical geometry. CitcomT is a transformed version of the 3-D Cartesian finite-element code, Citcom, originally described by Moresi & Solomatov (1995), Moresi & Gurnis (1996) and Zhong *et al.* (1998). Development of the Cartesian Citcom code of Zhong & Gurnis (1996) includes faults, a fully parallelized implementation and extensive benchmarking. So rather than create a completely new code with these same features in spherical geometry, we apply a coordinate system transformation to take advantage of these features in spherical coordinates. CitcomT gives nearly identical results to CitcomS (Zhong *et al.* 2000), a more traditional finite-element implementation of spherical flow without faults (see below).

For incompressible flow with an infinite Prandtl number and a Boussinesq approximation, the momentum and continuity equations are:

$$\sigma_{ij,j} + \rho g \delta_{i3} = 0, \tag{A1}$$

and

$$u_{i,i} = 0, \tag{A2}$$

with summation over repeated indices. $\sigma_{ij,j}$ is the spatial derivative of the stress tensor, σ_{ij}, $u_{i,i}$ is the spatial derivative of the velocity vector, u_i, and ρ and g are the density and gravitational acceleration. Eqs (A1) and (A2) can be expressed in matrix form for each element within the computational domain (Hughes 1987):

$$KU + G^{\mathrm{T}} P = F, \tag{A3}$$

and

$$GU = 0, \tag{A4}$$

where K is the stiffness matrix, which for the 3-D case with eight nodes and trilinear shape function, has 24×24 entries, G^{T} and F are the divergence and force vectors, P is the pressure (constant within each element), $U \equiv (\ldots, u_x^i, u_y^i, u_z^i, \ldots)$ is the velocity and $i = 1$–8 is the local node index.

The velocity in spherical coordinates, U', is related to the velocity in Cartesian coordinates, U, by the transformation,

$$U = RU', \tag{A5}$$

where R is a 24×24 matrix with eight 3×3 submatrices along the diagonal for each local node given by

$$R_i = \begin{pmatrix} \cos\phi & \cos\theta\sin\phi & -\sin\theta\sin\phi \\ -\sin\phi & \cos\theta\cos\phi & -\sin\theta\cos\phi \\ 0 & \sin\theta & \cos\theta \end{pmatrix}. \tag{A6}$$

The momentum and continuity equations are transformed to spherical coordinates by substituting (A5) into (A3) and (A4) and multiplying (A3) by R^{T}:

$$K'U' + G'^{\mathrm{T}} P = F', \tag{A7}$$

and

$$G'U' = 0, \tag{A8}$$

where $K' = R^{\mathrm{T}} KR$, $G' = GR$ and $F' = R^{\mathrm{T}} F$.

In practice the model is formulated in spherical coordinates. The transformation matrix for each node is formed and the mesh coordinates are then transformed to Cartesian coordinates. The matrices K, G^T and F are constructed in Cartesian coordinates. The transformation of K, G^T and F to spherical coordinates is then applied and the equations are solved in spherical coordinates.

A1 Faults in spherical coordinates

The matrix equations for faulted nodes in the Cartesian code are solved in a local coordinate system aligned with the fault surface (Zhong *et al.* 1998). This change of coordinate system is also achieved by a transformation of eqs (A3) and (A4) from the global Cartesian coordinate system to a local coordinate system that differs for each faulted element. In this case the 24×24 entry transformation matrix Γ has only one non-zero submatrix, T:

$$T = \begin{pmatrix} n_1 & n_2 & n_3 \\ t_1 & t_2 & t_3 \\ s_1 & s_2 & s_3 \end{pmatrix}, \tag{A9}$$

where $\hat{n}$, $\hat{t}$ and $\hat{s}$ are the normal and tangential vectors to the fault plane.

To apply the transformation to spherical coordinates to faulted elements, we first apply the spherical transform R to the fault transform matrix Γ,

$$\Gamma_r = R\Gamma. \tag{A10}$$

Then, we apply the transformation from spherical to fault-oriented coordinates to eqs (A7) and (A8):

$$K_\mathrm{f}' U_\mathrm{f}' + G_\mathrm{f}'^\mathrm{T} P = F_\mathrm{f}', \tag{A11}$$

and

$$G_\mathrm{f}' U_\mathrm{f}' = 0, \tag{A12}$$

where $K_f' = \Gamma_r^\mathrm{T} K' \Gamma_r$, $G_f' = G' \Gamma_r$, $F_f' = \Gamma_r^\mathrm{T} F'$ and U_f' is the velocity in the spherical-fault-oriented coordinate system. The velocity in spherical coordinates is given by $U' = \Gamma_r U_f'$.

APPENDIX B: DYNAMIC TOPOGRAPHY BENCHMARK

The geoid in a dynamic Earth is the result of the small difference between the large contributions from internal density anomalies and density anomalies from dynamic topography on boundaries, requiring accurate calculation of dynamic topography. Therefore, we need to verify that the topography calculation in CitcomT is capable of handling large variations in viscosity, both radially and laterally. However, CitcomT is only capable of modelling part of a sphere, limiting the analytic solutions available to conduct these benchmarks. Specifically, analytic solutions exist for topography caused by a harmonic load at depth, with a radial viscosity structure for a full sphere (Hager & O'Connell 1981), but there is not a similar solution for part of a sphere. Similarly, there exist analytic solutions for strong lateral variations in viscosity in Cartesian coordinates (Zhong 1996), but not in spherical coordinates. Therefore, special consideration is needed to apply these types of benchmarks to the particular geometry and boundary conditions used in CitcomT.

B1 Long-wavelength topography and radial viscosity structure

Since the spherical geometry of CitcomT is achieved as a result of the transformation of a Cartesian code (see Appendix A), the mesh boundaries follow lines of equal latitude and longitude within a region of a sphere. The sidewalls of the region are subject to zero shear stress boundary conditions. These are *natural* reflecting boundary conditions in the east–west direction (e.g. a domain spanning 180° in longitude reflected once completes the sphere). However, in the north–south direction the rectangular elements become highly distorted near the pole as lines of equal longitude become closer together, which could lead to errors in topography near the poles. In addition, these boundary conditions force the topography to have zero slope at the sidewalls.

To test the topography calculation with radial viscosity variations, we would like to use the analytic results available for a full sphere (Hager & O'Connell 1981). These results use spherical harmonics to express lateral variations in the density and propagator techniques to solve for dynamic topography $h(\theta, \phi)$ at the top or bottom boundary, expressed in terms of the harmonic coefficients given by

$$\delta h_{lm}^i = \frac{1}{\Delta \rho_a} \int_c^a H^l(r) \delta \rho_{lm}^i(r) \partial r, \tag{B1}$$

and

$$h(\theta, \phi) = \sum_{lmi} \delta h_{lm}^i Y_{lm}^i(\lambda, \phi), \tag{B2}$$

where l and m are the harmonic degree and order, respectively, $\delta \rho_{lm}^i(r)$ are the harmonic coefficients for the density anomaly, δh_{lm}^i are the harmonic coefficients for the topography, $H^l(r)$ is the displacement kernel for the top ($r = a$) or bottom ($r = c$) surface, which depends on the radial viscosity structure, $Y_{lm}^i(\lambda, \phi)$ are the spherical harmonic functions and λ is colatitude.

The boundary conditions on the regional model preclude direct comparison with the analytic solution; therefore, we use an indirect method to benchmark the topography calculation. First, we compare topography from CitcomS (Zhong *et al.* 2000), a fully spherical finite-element code, with the analytic solution for two-layer viscosity structures and a harmonic density anomaly at a single depth ($0.25a$). Unlike CitcomT, CitcomS uses an equal-area arrangement of elements that accounts for the pole and does not have sidewalls. Secondly, we compare topography from CitcomT with topography from CitcomSr. CitcomSr is a regional finite-element code otherwise identical to CitcomS. We use the same viscosity structures and density anomaly in a 45×45 deg^2 region. The model topography in these two steps is calculated, using the standard pressure smoothing technique (Hughes 1987), from the normal stress on the boundary ($h = \tau_{rr}/g\Delta\rho$). CitcomT is also able to calculate surface normal stress using the consistent boundary flux (CBF) method (Zhong *et al.* 1993). This method has higher accuracy than the pressure smoothing technique, in particular when variations in viscosity are present near the boundaries. Therefore, the final step is to compare topography from the pressure smoothing technique with topography from the CBF method for CitcomT. The results of this indirect test of the accuracy of the topography calculation are presented in Table B1. This approach relies on the initial benchmark of CitcomS to the analytic solution and the fact that CitcomS and CitcomSr are identical codes except for the boundary conditions.

Errors are less than 1 per cent for all tests except the comparison of the CBF and standard pressure smoothing technique in CitcomT for the models with a large jump in viscosity two elements from the top surface (models 3f and 3g). This error agrees with previous results

Table B1. Models used in the three-step benchmark of the long-wavelength topography with a two-layer radial viscosity structure. r_{η_1} is the radius of the boundary between the viscosity layers with values η_1 and η_2 for the top and bottom layers. δh_t per cent and δh_b per cent are the L_2-norm percentage errors for the top and bottom boundaries. 1a–e compare CitcomS with the analytic solution for an $l = 4$, $m = 4$ harmonic density anomaly at a depth of 1600 km over a full sphere (resolution is $1°$). 2a–e compare CitcomT with CitcomSr for the same load over a 45×45 deg^2 region of a sphere (resolution is $1°$). 3a–g compare CitcomT results using the CBF and pressure smoothing technique.

Model	r_{η_1}	η_1/η_2	δh_t (per cent)	δh_b (per cent)
	Topography benchmarks for radial viscosity variations			
1a	–	1	0.71	0.91
1b	0.75	100	0.65	1.34
1c	0.75	10 000	0.67	1.12
1d	0.926	100	0.83	0.63
1e	0.926	10 000	0.84	0.70
2a	–	1	0.09	0.27
2b	0.75	100	0.05	0.47
2c	0.75	10 000	0.06	0.63
2d	0.926	100	0.11	0.26
2e	0.926	10 000	0.10	0.26
3a	–	1	0.23	0.66
3b	0.75	100	0.28	0.60
3c	0.75	10 000	0.27	0.55
3d	0.926	100	0.62	0.56
3e	0.926	10 000	0.63	0.56
3f	0.9706	100	1.47	0.61
3g	0.9706	10 000	1.52	0.60

Table B2. Comparison of CitcomT topography with the analytic solution for a columnar viscosity structure. η_1/η_2 is the ratio of the viscosity in the two columns. η_1 is the viscosity for $x = 0.05$–0.1. δh_t per cent and δh_b per cent are the L_2-norm percentage errors for the top and bottom boundaries, respectively.

Model	η_1/η_2	δh_t (per cent)	δh_b (per cent)
	Topography benchmarks for lateral viscosity variations		
4a	1	0.037	0.11
4b	10	0.68	0.69
4c	100	0.80	0.81
4d	1000	0.82	0.82
4e	10 000	0.82	0.82
4f	1×10^5	0.82	0.82
4g	1×10^6	0.81	0.82

for Cartesian models that demonstrate the CBF method is more accurate for models with viscosity variations near the boundaries (Zhong *et al.* 1993). Although this three-step approach is not ideal, the consistently low errors at each step support our conclusion that the long-wavelength topography, subject to the boundary conditions in the regional model, are accurately determined for models with strong ($10^4\times$) radial variations in viscosity.

B2 Short-wavelength topography and lateral viscosity structure

Strong lateral variations in viscosity may occur at plate boundaries owing to variations in material properties and locally high stresses leading to short-wavelength topography. To test the accuracy of the CitcomT finite-element solution for models with strong lateral variations in viscosity, we use the exact analytic results for a columnar viscosity structure (a single jump in viscosity at the horizontal mid-point of the box) for 2-D incompressible Stokes flow in a box with reflecting boundary conditions on the sidewalls and free-slip boundary conditions on the top and bottom surface (Zhong 1996). The buoyancy is given by $\delta\rho(x', z') = -\sin(k_z z') \cos(k_x x)$ in a unit aspect ratio box. In spherical coordinates, x corresponds to longitude, ϕ, and z is depth. In these benchmarks, viscosity is explicitly set within each element to avoid large variations in viscosity within a single element.

In order to use these Cartesian solutions to benchmark CitcomT in spherical coordinates, we limit the width of the model domain to less than $0.1°$ on a 2-D transect at the equator. By limiting the size of the box, we insure that difference in lengths, volumes or areas arising from the different coordinate systems are insignificant. Results are presented in Table B2 for viscosity jumps up to 6 orders of magnitude. Errors are less than 1 per cent for all the models, demon-

strating the accuracy of the CitcomT solution for short-wavelength topography owing to lateral variations in viscosity.

APPENDIX C: INPUT BUOYANCY

The buoyancy of the slab is due mainly to the thermal structure of the slab. Ideally, we would like to derive the thermal structure of the slab starting with the temperature structure of the lithosphere and letting the temperature and flow evolve dynamically with a given viscosity structure. However, our understanding of the dynamics and the viscosity structure is not yet at the point where this kind of model can be used to recreate the morphology of a particular slab. While the viscosity structure and time dependence of subduction will influence the flow and the path the subducting slab takes to reach its present-day position, the temperature of the slab will not depend greatly on the details of the path as diffusion will act to smooth the overall temperature distribution.

While the particular path of slab descent has little affect on the final thermal structure, the boundary conditions and nature of the flow are important. Specifically, the thermal anomaly should be conserved: the total thermal anomaly of the slab and surrounding mantle must be equal to the total thermal anomaly in the lithosphere before subduction. Models that assume isothermal boundary conditions on the surface of the slab (McKenzie 1969) have a net loss of thermal anomaly, leading to an underestimate of the slab buoyancy at depth.

We estimate the steady-state thermal structure of the slab using a kinematic model of the flow in the slab and surrounding mantle based on the analytic solution for viscous flow in a corner, known as corner flow (Batchelor 1967). The magnitude and distribution of the flow are completely determined by the geometry and slab velocity, U, and do not depend on the viscosity of the fluid because the solid boundaries have infinite viscosity. This renders the effect of the viscosity of the fluid, for any magnitude, small in comparison. This is, of course, different from flow in the mantle, for which the viscosity of the slab may only be a few orders of magnitude greater than the surrounding mantle and the viscosity of the surrounding mantle may not be homogeneous. Nonetheless, corner flow does simulate many features of the flow observed in dynamic models, including the large-scale corner flow above and below the slab and broadening of the flow and boundary layer above the slab with depth.

To estimate the thermal structure of the Tonga–Kermadec slab, the position of the top of the slab is assumed to lie along the top surface of seismicity within the slab, extending from the surface to a depth of approximately 670 km. Since, it is not known whether these earthquakes occur within the core of the slab or along the top

surface of the slab, this assumption may introduce a small shift in the position of the slab, by up to 25 km (assuming a 100 km thick slab), for depths below the lithosphere. Below the top surface of the slab, the flow is given by the corner flow solution with a dip angle, $\theta_0 \geq 90°$. The flow above the slab is given by the corner flow solution with a dip angle, $\theta_0 \leq 90°$, except for the top 100 km, which is held fixed. Since the dip of the slab varies with depth, the flow at a given depth is determined using the local dip of the slab. The resulting field is not strictly divergence-free, but the errors are small and do not affect the thermal structure. The velocity of the slab is fixed at an average rate of subduction based on plate reconstructions (Müller *et al.* 1993), approximately 5–10 cm yr^{-1}. The initial thermal structure of the lithosphere is defined as a half-space cooling profile for the age of subducting crust at the start of subduction. For Tonga the initial age of the subducting lithosphere is ~50 Ma with some variation along strike of the trench (Billen & Stock 2000). The thermal structure is then calculated from the advection–diffusion equation for the defined velocity field, using the finite-difference method, until a steady state is reached (approximately 25 Myr). The finite-difference calculation is performed on a high-resolution (5 km) mesh extending from the surface to a depth of 800 km and 45° in longitude and latitude. The temperature field is then interpolated on to the distorted finite-element mesh. An example of the velocity field and thermal structure are given in Fig. C1.

APPENDIX D: BEHAVIOUR OF A LOW-VISCOSITY REGION: 2-D TEST CASES

To understand the effect of a spatially confined, low-viscosity zone (LVZ) on topography and flow in the complex setting of a subduction zone, it is necessary to first consider some simple geometries. We present results for three geometries in two dimensions that allow us to examine the influence of the relative position of the LVZ and a density anomaly with radial- and temperature-dependent variations in viscosity.

Fig. D1 A illustrates the three geometries used. In all models the LVZ is in the same position, 50 km from surface, 200 km wide and 150 km high. The position of the 2-D cylindrical density anomaly is shifted relative to the LVZ, placing it either next to the LVZ
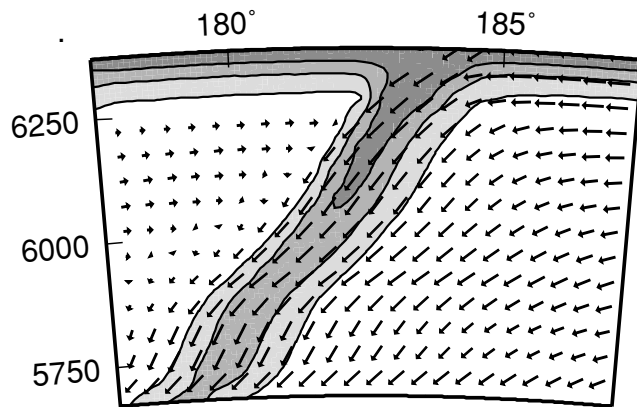
Figure C1. East–west cross-section of the corner flow velocity field used to calculate the input buoyancy field for the Tonga–Kermadec slab at 28°S. The flow consist of two corner flow solutions above and below the top surface of the slab, with a maximum slab flow rate of 10 cm yr^{-1}. The steady-state temperature field results from ~ 25 Myr of subduction. The contour interval is 400 °C.
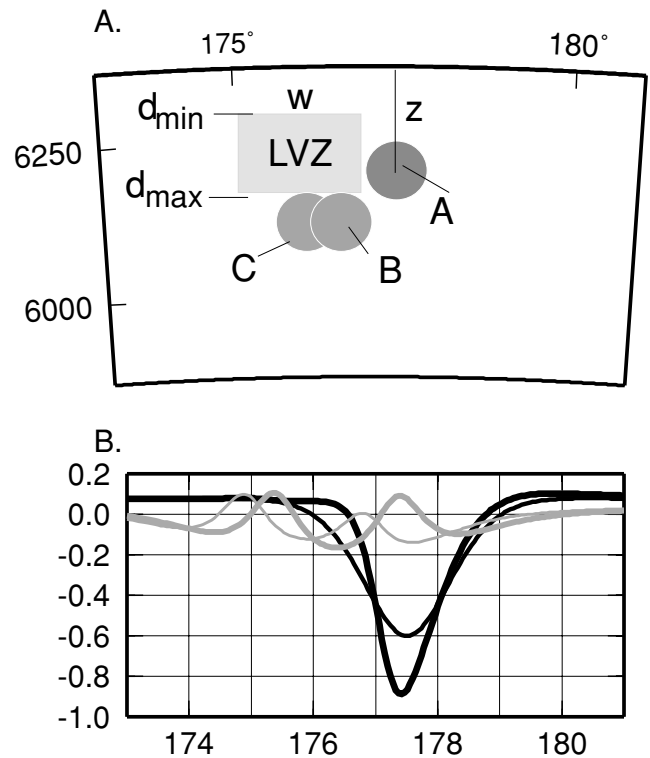
Figure D1. (a) Geometry of LVZ and density anomaly used to investigate the effect of the LVZ on topography and flow. The LVZ position is fixed with $d_{min} = 50$ km, $d_{max} = 200$ km and $w = 200$ km. The density anomaly can occupy three positions: A, next to the LVZ at $z = 150$ km; B, below the right-hand corner of the LVZ at $z = 250$ km; C, centred below the LVZ at $z = 250$ km. (b) Topography profiles for models with a strong cylinder, lithosphere and lower mantle. Thin black line: cylinder in position A, without an LVZ. Thick black line: cylinder in position A, with LVZ. Thick grey line: cylinder in position B, with LVZ. Thin grey line: cylinder in position C, with LVZ.

(position A, $z = 150$ km), below the LVZ under the right-hand corner (position B, $z = 250$ km) or centred under the LVZ (position C, $z = 250$ km). These three positions are used to understand how the relative position of the slab and a low-viscosity region in the wedge will influence topography and flow. The viscosity of the LVZ is 100 times less than the surrounding asthenosphere (reference viscosity is 3×10^{20} Pa s, used to dimensionalize topography and velocity). The density anomaly of the sphere is 50 kg m^{-3}. For each position of the density anomaly, we tested four viscosity models:

(1) uniform viscosity, including the dense cylinder (except for the LVZ when it is present);
(2) strong cylinder, with the cylinder viscosity, $\eta_{cyl} = 20\eta_o$;
(3) strong cylinder with strong lithosphere ($z = 100$ km), $\eta_{lith} = 100\eta_o$;
(4) strong cylinder with strong lithosphere and lower mantle ($z > 700$ km), $\eta_{lm} = 100\eta_o$.

The results for viscosity model with a strong cylinder, lithosphere and lower mantle (4) are presented in Figs D1(b) and D2. For comparison we also calculate the flow and topography for each viscosity structure without the LVZ. In these cases the cylinder is in position A. The relative position of the LVZ and density anomaly has a large influence on both the flow and the topography. Without the LVZ the topography is symmetrically centred on the cylinder, 0.6 km deep and 200 km wide. For a cylinder in position A with an LVZ, the
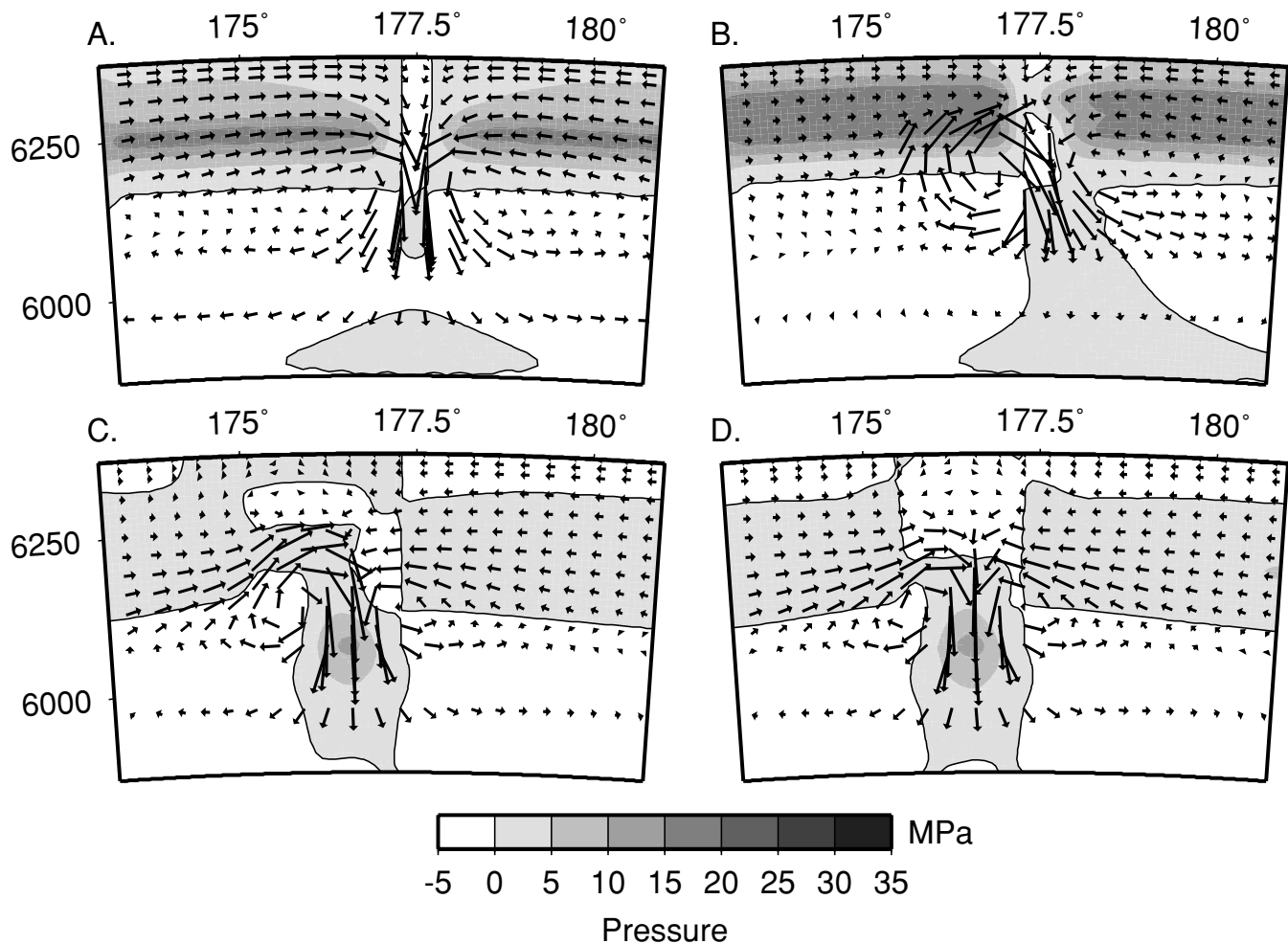
Figure D2. Pressure and flow for models with a strong cylinder, lithosphere and lower mantle (4). Velocity is scaled by the maximum velocity in each model. (a) Model with no LVZ, with the cylinder in position A ($v = 0.2$ cm yr^{-1}). (b) Cylinder in position A, with an LVZ ($v = 0.3$ cm yr^{-1}). (c) Cylinder in position B, with LVZ ($v = 0.8$ cm yr^{-1}). (d) Cylinder in position C, with LVZ ($v = 0.8$ cm yr^{-1}).

topography above the LVZ is diminished, while the topography directly above the cylinder deepens. For cylinders in position B and C the topography is reduced dramatically, to less than 0.2 km, with a small bit of asymmetry for position B (slightly deeper directly above the cylinder). For models with a strong lithosphere two topography highs occur above the corners of the LVZ.

The change in topography caused by the LVZ is a result of the change in the pressure field and flow, with the largest effect being caused by changes in the pressure field. For models without an LVZ, the density anomaly creates a region of low dynamic pressure above it, reaching all the way to the surface (light grey regions in Fig. D2). This low-pressure region near the surface draws the flow horizontally along the top surface and down directly above the density anomaly, creating a large stress on the surface. Adding an LVZ next to the density anomaly makes the region of low pressure above the density anomaly narrower and increases its magnitude. The flow also becomes asymmetric. In the case shown in Fig. D2(b), a local return flow forms, arising from the strong lower mantle and

lithosphere. If the viscosity is uniform outside the LVZ (viscosity structure 1), the flow has a larger upward component of flow than the case without an LVZ, but the flow below the density anomaly remains fairly symmetric and directed downward.

Placing the density anomaly below the LVZ (Fig. D2c and d) effectively shields the surface from the low-pressure region above the density anomaly. Instead of reaching all the way to the surface, the low-pressure region is concentrated in the LVZ, creating a region of higher pressure above the LVZ. Models with the cylinder in position C also have asymmetric flow, with higher velocities and local return flow in the LVZ. Models with the cylinder in position D have symmetric flow and local return flow on both sides of the density anomaly. The two topography highs above the corners of the LVZ, in models with the cylinder beneath the LVZ (Fig. D1b, grey lines), are caused by pressure concentrations at the corners caused by the rapid change in viscosity radially and laterally. These topographic highs can be reduced by making the transition of viscosity across the LVZ boundary more diffuse.